

Montclair State University

Montclair State University Digital Commons

Theses, Dissertations and Culminating Projects

5-2015

Numerical Study of Body Shape and Wing Flexibility in Fluid Structure Interaction

Peter Nolan

Follow this and additional works at: <https://digitalcommons.montclair.edu/etd>



Part of the [Mathematics Commons](#)

MONTCLAIR STATE UNIVERSITY

/ Numerical Study of Body Shape and Wing Flexibility in Fluid Structure Interaction /

by

Peter Nolan

A Master's Thesis Submitted to the Faculty of

Montclair State University

In Partial Fulfillment of the Requirements

For the Degree of


Master of Science

May 2015


College of Science and Mathematics

Department of Mathematical Sciences

Thesis Committee



Thesis Sponsor: Dr. Ashwin Vaidya



Committee member: Dr. Bong Jae Chung



Committee member: Dr. Bogdan Nita

Numerical Study of Body Shape and Wing Flexibility in Fluid Structure Interaction

Abstract

We discuss the equilibrium configurations of fibers clamped to an ellipsoidal body and immersed in a flow ranging between 0-50 cm/s. Experimental and numerical results are presented and the effects of flow speed, body shape, and orientation of the fibers upon the equilibrium configuration are investigated. Our investigations reveal that the orientation of the fibers, the length of the length fibers, as well as, the shape of the body has a significant impact upon the bending and drag experienced by the ellipsoid-fiber system. We note that (i) less eccentric bodies experience greater drag forces and increased bending of the attached fibers, (ii) the fibers oriented with the flow experienced less drag and bending than the fibers oriented perpendicular to the flow, (iii) the longer fibers bend significantly more than the shorter ones, and (iv) the longer fibers display oscillatory or flapping motion at much lower flow speeds than their shorter counterparts. The simulations also reveal that the drag on the fiber is noticeably affected by the size of the basal body. Drag exponents (or Vogel exponents) are also computed and seen to deviate slightly from previous results.

NUMERICAL STUDY OF BODY SHAPE AND
WING FLEXIBILITY IN FLUID STRUCTURE
INTERACTION

PETER JOSEPH NOLAN

A MASTERS THESIS SUBMITTED IN PARTIAL FULFULLMENT
FOR THE DEGREE OF MASTER OF SCIENCE

DEPARTMENT OF
MATHEMATICAL SCIENCES
ADVISER: DR. ASHWIN VAIDYA

MONTCLAIR STATE UNIVERSITY
MONTCLAIR, NJ
MAY 2015

© Copyright by Peter Joseph Nolan, 2015.
All rights reserved.

Acknowledgements

I would like to thank my parents for never giving up on me. I would like to thank Ryan Allaire for allowing me to intellectually leech off him for the past two years. I would like to thank my advisor, Dr. Vaidya, whose sage wisdom has guided me, and led to my being accepted into a Ph.D. program. I would like to thank my thesis committee members, Dr. Nita and Dr. Chung, for taking the time to assist me in writing this thesis.

I would like to thank Dr. Jeffrey Scott Dwoskin for creating the \LaTeX template for the Princeton University thesis. I would like to extend my thanks the Math department at Princeton University for providing the original `documentclass` file that this thesis class was based upon. I would also like to thank Andrew Mauro, for getting this \LaTeX template functional for our research group. His hard work has undoubtedly saved me countless hours of frustration.

To Myself, I couldn't have done it without you.

Contents

Abstract	iii
Acknowledgements	iv
List of Tables	vii
List of Figures	viii
1 Introduction	1
2 Experiments	9
3 Governing Equations	17
4 Numerics: Single Fiber Equilibrium Configuration	20
4.1 Set Up	21
4.2 Convergence tests	22
4.3 Results: comparison with experiments	24
5 Numerics: Optimal Body Shape with Two Fibers	31
5.1 Set up	32
5.2 Biological Models	33
5.3 Convergence Tests	36
5.4 Checks for Accuracy	39
5.5 Results	41
5.6 Biologically Relevant Results	43
6 Conclusion	54
7 Bibliography	57
A Numerical Parameters: Equilibrium Configuration	60
B Numerical Parameters: Optimal Body Shape	61
C High Definition Images	63
D Bending Comparisons	68
E Drag Comparisons	71

List of Tables

4.1	Critical flow speeds at which the fibers display periodic oscillations. . . .	26
4.2	The drag exponents for fibers of varying lengths and orientations based on least squares fit of our 2D simulations.	27
5.1	The dimensions of the ellipsoidal bodies used, in centimeters.	32
5.2	Dimensions of the biological models in centimeters.	36
5.3	Comparison of the time taken to perform each numerical simulation arranged by mesh density.	38
5.4	Results of the benchmarking simulations. The Computed Drag Coefficient is the value that was calculated from the results of these benchmarking simulations. The Cortes' Drag Coefficient is what was reported by Cortes et al. The Literature Drag coefficient is from the existing literature. The Error vs Lit is the percent error in our computed Drag coefficient versus that found in the literature.	40
5.5	The drag exponents for bodies of varying eccentricities and fiber orientations based on least squares fit of our 2D simulations.	43
A.1	The table lists the numerical values of parameters assumed in the Equilibrium Configuration numerical investigations.	60
B.1	The table lists the numerical values of parameters assumed in the Optimal Body Shape numerical investigations.	62

List of Figures

2.1	Picture of the flow tank that was used for these experiments. The flow goes from left to right.	10
2.2	Experimental setup: panel (a) shows a side view of the fiber attached to the spherical body, (b) shows a rear view of the same object and panel (c) shows the nylon fiber inserted into the styrofoam ball which serves as a basal body. The flow direction in the experiments occurs from left to right in panel (a) or out of the plane of the paper in panel (b).	11
2.3	These graphs show the average bending of the fibers between their suspension point and free end based on experimental investigations. Variations of the bending with $\tilde{C}a$, fiber length and initial orientation are examined. Panel (a) corresponds to $\theta_0 = 225^\circ$, (b) to $\theta_0 = 270^\circ$, (c) to $\theta_0 = 315^\circ$. . .	13
2.4	Visualization of the wake vortex behind the fiber. Panel (a) shows the vortex structure for a 4 cm fiber at approximately $U=5$ cm/s while panel (b) shows the structure for a 6 cm fiber at a higher velocity of $U=15$ cm/s.	14
2.5	An artistic representation of the flow tank showing the x, y, and z axes, along with the direction of the flow, and how θ was measured.	14
2.6	The image shows the wake vortex behind the obstacle in the Z direction. The fiber used here is 6 cm in length and the corresponding flow velocity is nearly 15 cm/s. The picture in the red box shows the three dimensionality of the wake flow field. The fuzzy circular region behind the sphere corresponds to the 3d wake structure behind the sphere; the fiber however does not generate any noticeable wake in the third dimension.	16
4.1	The two-dimensional user controlled mesh generated for the fluid structure problem under investigation	22
4.2	The values for drag and lift are computed for a 4 cm fiber of thickness 0.05 cm with an initial orientation of $\theta_0 = 270^\circ$ relative to the flow as a function of different mesh densities. Here the x-axis denotes the various mesh configurations, where 1 is defined as a user controlled mesh, 2 as 'coarser', 3 as 'coarse', 4 as 'normal', 5 as 'fine', 6 as 'finer', 7 as 'extra fine', and 8 as 'extremely fine'.	23
4.3	The values for drag and lift are computed for a 4 cm fiber with initial an orientation of $\theta_0 = 270^\circ$ relative to the flow, as a function of different channel widths.	24

4.4	The time evolution of a 4 cm fiber at various orientations are depicted along with the corresponding flow structure. The fibers achieve their steady configurations as the flow simultaneously evolves into its steady state. The wake vortex structure is also seen to depend on the fiber orientation.	28
4.5	These graphs show the average bending of the fibers, between their suspension point and free end, versus $\tilde{C}a$ for three different fiber lengths and initial orientations, based on the 2d numerical simulations. The triangular points refer to the 4cm case where the body was reduced in size. Panel (a) corresponds to $\theta_0 = 225^\circ$, (b) to $\theta_0 = 270^\circ$, (c) to $\theta_0 = 315^\circ$	29
4.6	The panels (a), (b), and (c) show variations in drag versus U. Panel (d) shows the drag transition of a sample case, the 4 cm fiber at $\theta = 270^\circ$. In all cases here, the fiber is seen to reach steady state at about 1 s with the highest drag when the fiber protrudes into the flow and the least drag when the fiber is in its most streamlined configuration.	30
5.1	The two-dimensional triangular <i>fine</i> mesh generated in COMSOL for the fluid structure problem under investigation	37
5.2	Results of Mesh Convergence Study: drag force and deformation angle as functions of mesh density. 1 = 'Normal', 2 = 'Fine', 3 = 'Finer', 4 = 'Extra Fine', 5 = 'Extremely Fine'.	45
5.3	Results of Channel Height Convergence Study: drag force and deformation angle as functions of channel height. Channel height given in centimeters.	46
5.4	Models in steady state configuration	47
5.5	Velocity Versus Drag, by Eccentricity	48
5.6	Modified Cauchy Number Versus Bending, by Fiber Orientation	49
5.7	Drag Versus Fiber Orientation and Eccentricity. This graph shows that the drag force the ellipsoid-fiber system experiences is more strongly associated with the orientation of the fibers than the eccentricity of the body. Orientation 1: 90° , Orientation 2: 45° , Orientation 3: 45° fixed along the edge	50
5.8	Drag Versus Organism Eccentricity	51
5.9	Biological Model: Eccentricity vs Drag Force	51
5.10	Biological Model: Fiber Length vs Drag Force	52
5.11	Biological Model: Drag Vs Eccentricity and Fiber Length	53
C.1	0.00 eccentricity model with fibers at 45° fixed along the edge, at time 5 seconds	63
C.2	0.00 eccentricity model with fibers at 45° , at time 5 seconds	64
C.3	0.00 eccentricity model with fibers at 90° , at time 5 seconds	64
C.4	0.50 eccentricity model with fibers at 45° fixed along the edge, at time 5 seconds	65
C.5	0.50 eccentricity model with fibers at 45° , at time 5 seconds	65
C.6	0.50 eccentricity model with fibers at 90° , at time 5 seconds	66

C.7	0.99 eccentricity model with fibers at 45° fixed along the edge, at time 5 seconds	66
C.8	0.99 eccentricity model with fibers at 45°, at time 5 seconds	67
C.9	0.99 eccentricity model with fibers at 90°, at time 5 seconds	67

Chapter 1

Introduction

In this work we focus on the problem of equilibrium (re)configuration of deformable fibers in a fluid flow. Other than the well known engineering applications of this problem, flexible fluid-structure interactions are ubiquitous in nature and their biological applications are particularly interesting. The problem of snoring, for instance, has its roots in a fluid-structure interaction, where the fluid is air and the structure corresponds to the soft-palette in the pharynx whose oscillations induce snoring.¹⁵ A second widely studied application is the dynamics of ciliary hairs which line much of the human body and whose motion helps propel bodily fluids.²² The breakdown of the ciliary mechanism is the cause of several human pathologies and constitutes an important medical question. Fluid structure problems are also essential to our understanding of the mechanics of flying and swimming.⁶ The investigation of the positioning and orientation of wings, their length and equilibrium configurations, flapping modes, can all assist in optimal flight design. In the context of plant biology, the pioneering work by Vogel²⁸⁻³⁰ has lead to considerable attention to issues of forces experienced by plants in high winds.^{14,18} The flexibility of plants and aquatic vegetation can provide important clues of their health.

The fundamental phenomenon of the terminal state, including velocity and orientation, of a rigid body in a fluid flow is a well studied problem for over a century. Despite the overabundance of attention to this problem, several significant fundamental questions remain unanswered. In the past few decades, some effort has been spent on explaining the terminal orientation of rigid symmetric bodies in a flow (where the structure is freefalling or hinged with one degree of rotational freedom).^{5,9-11,16,17,21,27,31} Previous studies on hinged cylinders reveal that when the flow speed (or Reynolds number) is very low, the cylinder maintains its initial orientation. However as the Reynolds number exceeds a certain threshold, determined by the inertia in the system, the cylinder aligns its longest axis perpendicular to the direction of the flow which is a new stable equilibrium. Beyond a second threshold for the Reynolds number, the particle begins to display complex unsteady behavior such as periodic oscillations and autorotation.^{5,19,21} These varying orientations of a rigid body have a lot to do with the structure of the vortex shedding around the body. When the suspended body has the additional characteristic of being flexible, the physics becomes even more complicated.

The current thesis is a part of our ongoing contribution to the broader subject of terminal orientations and configurations in fluid-solid interaction and aims on extending our previous work to flexible systems. In a series of fundamental experimental and theoretical papers on similar subjects^{1,12,25,30,32} and others, it has been pointed out that deformable bodies in a flow bend in order to reduce drag.

Drag is "a force acting on a moving body, opposite in direction to the movement of the body, caused by the interaction of the body and the medium it moves through."⁸ In this case the medium is a fluid and instead of the body moving through the fluid, the fluid is

moving across the body. Mathematically, drag is defined as

$$F_d = \hat{\mathbf{u}}_{\parallel} \cdot \oint_S \mathbf{T} \cdot \mathbf{n} dS \quad (1.1)$$

where F_d is the drag force, $\hat{\mathbf{u}}_{\parallel}$ is the unit vector in the direction of the fluid flow, S is the surface of the body, \mathbf{T} is the Newtonian stress tensor, \mathbf{n} is the normal unit vector pointing into the body. Typically drag is calculated using the formula

$$F_d = \frac{1}{2} \rho u^2 C_d L \quad (1.2)$$

where ρ is the density of the fluid, u is the speed of the fluid flow, C_d is the drag coefficient of the body, and L is the length of the body. However, this formula was developed based on rigid bodies. In flexible bodies drag is

$$F_d = \frac{1}{2} \rho u^\alpha C_d L \quad (1.3)$$

where α is the drag or Vogel, exponent and varies between $1 < \alpha < 2$ depending on the stiffness of the body.²⁸⁻³⁰

Luoding Zhu³² investigated how dimensionless flow parameters influence vortex shedding. Zhu was interested in how different values of the parameters influence vortex shedding simulations at Reynolds numbers between 30 and 800. In particular Zhu investigated the Reynolds number, the dimensionless fibre flexure modulus, and the dimensionless fibre length. The effects of each of these parameters is investigated individually. Zhu's investigations were performed using numerical simulations.

From his simulations Zhu concluded that "the Reynolds number has a significant influence on vortex shedding and fibre vibration."³² The higher the Reynolds number,

the more vortex shedding and fibre vibration occurred. Zhu also found that "the fibre dimensionless flexure modulus has a significant influence on vortex shedding, [and] fibre vibration..."³² The lower the flexure modulus, the less vortex shedding and fibre vibration occurred. Furthermore, "the dimensionless fibre length has a significant influence on vortex shedding, [and] fibre vibration..."³² The longer the fiber length the more vortex shedding and fibre vibration occurred.

Silas Alben, Michael Shelly, and Jun Zhang¹ investigated the reduction of drag on a flexible fiber as it is bent by a fluid flow. They performed experimental work which they then compare to theoretical computations.¹ Their primary interest concerns values of η , which is defined as the ratio of "fluid kinetic energy to elastic potential energy, or the ratio of fibre length to an intrinsic 'bending length'..."¹

Alben et al.¹ found that for values of η significantly smaller than one the fiber remains straight. However, as η approaches $O(1)$, a transition to bending occurs and there emerges a self-similarity in the fiber's shape. As η grows significantly larger than one the "large curvature becomes confined to an ever-smaller region near the tip..."¹ Alben et al.¹ concluded that the theoretical and experimental models give similar drag results for objects with similar shapes and that bending and fluid pressure are sufficient to describe the observed reduction of drag.

Michael J. Shelley and Jun Zhang²⁵ reviewed previous experimental studies on the flapping of flexible bodies in flow, most notably studies by Taneda in the 1960s. Building off of this review the paper then briefly discusses an experiment performed by Zhang. The paper then goes on to review theoretical studies in fiber flapping, most notably some of Zhang's work on variants of fiber flapping. Afterwards, the paper discusses the

flapping of flexible sheets. Zhang et al.²⁵ conclude their paper with a discussion of the outlook of the study of flapping bodies. The authors note that, because most of the current theoretical analysis has been in two dimensions, it will be challenge to move to three dimensional theoretical analyses. Furthermore, analyses based on numerical simulations will be particularly challenging.²⁵

L. A. Miller, A. Santhanakrishnan, S. Jones, C. Hamlet, K. Mertens, and L. Zhu²⁰ investigated how the reconfiguration of a leaf in a fluid flow contributes to the reduction of vortex induced vibrations. Because plants can reconfigure their shape, they are able to withstand the mechanical stresses that result from fluid forces. This is of great interest in to those in the fields of comparative biomechanics, fluid dynamics and biologically inspired design. The reconfiguration of plants, and the effects that reconfiguration has on vortex induced vibrations were studied both experimentally and by the use of two dimensional numerical simulations.

Miller et al.²⁰ found that the wild violet and wild ginger leaves reconfigured into cones under the pressure of a fluid flow. This reconfiguration led to the creation of "a relatively stable pair of alternately spinning vortices"²⁰ in the wake of the leaves. Circular man made models also reconfigured into cones and developed vortices similar to those formed in the wake of the wild violet and wild ginger leaves. Square man made models were found to reconfigure into a U shape. This reconfiguration led to "strong oscillations and vortex shedding."²⁰ Furthermore, in the two dimensional simulations it was found that by adding the flexible tether to the flexible beam of the leaf, the drag force, the vortex shedding, and the oscillations were all magnified compared with similar numerical simulations. The authors concluded that more than just flexibility is needed for the reduction of drag forces, and that the shape of an object's reconfiguration under pressure

is important as well.

Thomas Barois and Emmanuel de Langre³ investigated whether or not it is possible for an object in a fluid flow to deform in such a way that the drag forces on that object are independent of the velocity of the fluid flow. Furthermore if this deformation is possible, does the independence of the drag force hold over a range of varying conditions. Specifically the case of membranes was considered, with an emphasis "on the cancellation of velocity dependence rather than on the minimizations of the drag at a given velocity."³ The authors noted that such behavior has been observed at low Reynolds numbers within the DNA molecule.

Barois and Langre found that, using a membrane, it was possible to create an object that would deform in such a way that the drag forces on that object are independent of the velocity of the fluid flow.³ Furthermore, the independence of the drag force was observed to hold for a range of velocities. The authors explain that this is because membranes only transmit tangential forces and the pressure of the fluid flow modifies the orientation of the membrane's in-plane tension, while not altering the magnitude of the in-plane tension.³ Though the authors do not explicitly state it, it appears that the drag force applied to the membrane becomes converted into a lift force thereby reducing the drag forces on the body and creating a body whose drag is independent of the velocity.

Steven Vogel³⁰ explained, among other topics, how leaves and leaf clusters deform in high velocity winds in order to reduce drag. Whereas previous studies into the effects of windiness on leaf configurations were focused on time averaged air flows, Vogel's work focused on how leaves reconfigured during brief gusts of wind. Vogel restricted his work to leaves and leaf clusters because "...on a fully leafed tree the drag of its leaves should

be the largest force."³⁰ Vogel notes that this information is even more important than the time averaged studies, since even a short period of intense drag can be a significant risk to a plant.

Vogel explains how leaves and leaf clusters reduce their drag by reconfiguration.³⁰ He observes that simple leaves curl up into cones as wind speed increases. When there is a cluster of simple leaves, this cluster can curl up into a conical shape. Vogel notes that while a cluster of leaves that can individually curl into cones will curl into a conical shape, just because a cluster of leaves curls into a conical shape does not guarantee that the individual leaves will curl into cones. Vogel also observed that pinnately compound leaves may curl up into cylinders. Meanwhile, clusters of leaves pinnately arranged on a branch might bend back on top of each other and stack up, thereby reducing their drag. Vogel also pointed out that all of the simple leaves which curl into cones share two features. First they have petioles which are longer than 2 cm. Second they have blades which have basal lobing. This lobing typically curls upward enabling the formation of cones as wind velocity increases.

In this thesis we investigate flexible fibers attached to a basal body. This is a triply difficult problem to investigate. This problem has a flexible solid attached to a rigid solid, all interacting with a fluid flow. This is a new and unexplored area in the field of flexible fluid-structure interaction. Prior to this all investigations of flexible fluid-structure interactions have looked at either stand alone, or tethered flexible structures. Both Alben et al. and Zhu looked at a stand alone flexible fiber in their investigations.^{1,32} Barois and Langre investigated a stand alone flexible membrane.³ Miller et al. looked at stand alone, as well as, tethered flexible structures.²⁰ Vogel investigated both stand alone leaves and clusters of leaves.³⁰ However, none have looked at a flexible structure attached to a basal body. A basal body is naturally present in all physical examples and therefore accounting

for it is essential.

Specifically, this thesis investigates flexible fibers attached to a basal body and submerged in a water tank with speeds 0-50cm/s. This investigation is performed both experimentally and through two dimensional numerical simulations. This thesis also looks into some other as yet unexplored aspects of the problem. The effects of fiber length, fiber orientation(θ_0), and the eccentricity of the basal body are all looked at. In particular this thesis looks at the effects these parameters have on drag, lift, and fiber deformation. Vogel, or drag exponents are also calculated.

The rest of this thesis is organized as follows. Chapter 2 describes the experimental investigations which were performed, including the procedure and outcomes. Chapter 3 details the equations which govern the numerical simulations. Chapters 4 and 5 explain the numerical studies performed using the software COMSOL Multiphysics. The details of the numerical scheme, convergence study and comparisons with experiments are presented. Detailed tables and images related to the numerical simulations can be found in the appendices.

Chapter 2

Experiments

Detailed experiments were conducted on the interaction of a suspended, clamped fiber in a flow as a function of the fiber length, initial orientation(θ_0) and flow speed (U). The experiments were performed in a flow tank with recirculating water with flow velocities ranging between 0-50cm/s ($0 < Re = \frac{\rho_f U L}{\nu} < 30,000$ where ρ_f is the density of the fiber, U is the free stream velocity measured at the center of the tank in the absence of an obstacle and L is the fiber length). Fibers chosen for our study were made of nylon and polyester and were extracted from paint brushes. The exposed portion of the fibers were of lengths 2cm, 4cm and 6cm. These were inserted into a styrofoam ball of diameter 3cm in such a way as to prevent any motion with respect to the ball (figure 2.2). The styrofoam ball with the fiber was held in place by means of a copper wire of thickness 1mm passing through the ball which was placed at the center of the tank appropriately to prevent any transverse or rotational motion. Panels (a) and (b) in figure 2.2 show a side and back view of the fiber with the spherical basal body to which it is attached.

The dynamics of the fiber in the flow were recorded using a digital camera (Sony α), placed orthogonal to the flow. The orientation of the fiber with respect to the flow

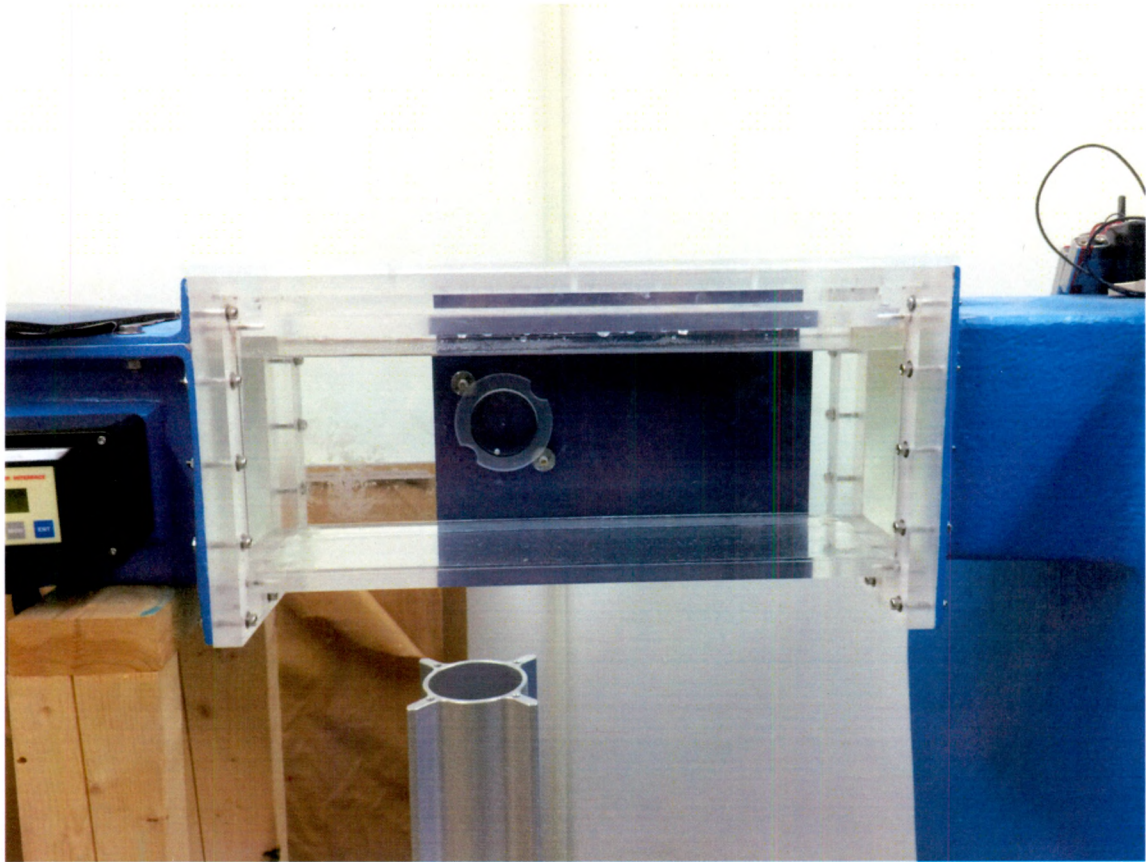


Figure 2.1: Picture of the flow tank that was used for these experiments. The flow goes from left to right.

were changed by appropriately rotating the styrofoam ball upon the copper wire before clamping it. In the present study three different angles were considered (where angles are measured using the standard convention with respect to the horizontal axis, counterclockwise.), namely¹ 225° , 270° and 315° .

The results of this experimental study are shown in figure 2.3. The primary experimental observation relates the bending of the various fibers as a function of the Cauchy number (Ca), which defines the ratio of inertial to elastic forces in the system. The Cauchy number was chosen over the Reynolds number because the Cauchy number takes into

¹In our numerical simulations for the problem, presented in the following section, the fibers were placed at the antipodal end of the spheres, i.e. at angles 135° , 90° and 45° . Due to the symmetry of the problem and absence of any gravitational effects on the fiber, these angles are similar to those used in experiments. However, henceforth in this text we will use the experimental angles when referring to the fiber orientation.

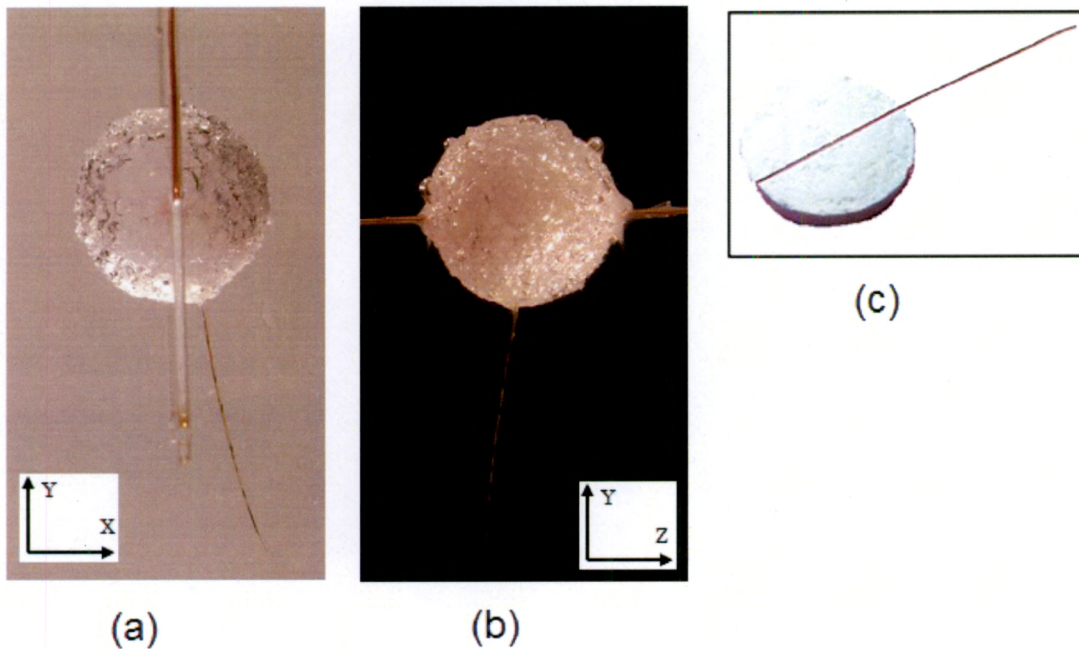


Figure 2.2: Experimental setup: panel (a) shows a side view of the fiber attached to the spherical body, (b) shows a rear view of the same object and panel (c) shows the nylon fiber inserted into the styrofoam ball which serves as a basal body. The flow direction in the experiments occurs from left to right in panel (a) or out of the plane of the paper in panel (b).

account the stiffness properties of the solid, whereas the Reynolds number only accounts for the properties of the fluid. The Cauchy number has been defined as $Ca = \frac{\rho U^2}{K}$ where ρ is the density of the fluid, U is the characteristic velocity and K is the bulk modulus of the fiber which is taken to be $4GPa$ in these experiments, corresponding to Nylon. Gosselin et al.¹² note that the drag on a flexible rectangular plate can be seen to depend on an appropriate scaling of Ca , defined by $\tilde{Ca} = C_D \cdot Ca$ (where C_D is the drag coefficient) such that for $1 < \tilde{Ca} < 10$ the flexible plate transitions to a reconfigured state. Due to the difficulty in obtaining drag coefficients and flexural rigidity in this study, a simple rescaling of the Cauchy number, $\tilde{Ca} = 10^{-12} \times Ca$ is used to bring it to the same scale as in previous studies.

Figure 2.3 shows the average bending of the fibers as a function of $\tilde{C}a$ for various dimensions of the fiber and different initial configurations. The average bending is estimated by the angle of the straight line connecting the points P and Q where P is the point on the fiber in contact with the ball and Q is the free end of the fiber. The bending is shown for the three fibers of different lengths as well as the initial orientation angle of the fiber (θ_0). Increasing $\tilde{C}a$ has the effect of greater bending force upon the fiber. Our observations reveal that beyond a certain critical value of $\tilde{C}a$, which depends upon the material of the fiber and its physical dimensions such as length and thickness, the fiber begins to bend and continues to do so until it reaches a second critical $\tilde{C}a$, which we shall refer to as $\tilde{C}a_c^{(2)}$, when it starts to display time dependent motion. Since the focus of this paper is the equilibrium configuration of the fiber, the $\tilde{C}a$ was restricted to the range below $\tilde{C}a_c^{(2)}$. The longer fibers display greater propensity to bending, and eventually flapping or random motion, than the shorter ones and start to bend for smaller values of $\tilde{C}a$ as seen from the slopes of the tangents to these curves; the 2cm fiber shows a minimal change with respect to its initial configuration.

The average bending is seen to be highest when the fiber protrudes more into the incoming flow ($\theta_0 = 225^\circ$) and least for the case of $\theta = 315^\circ$ where the fiber is closer to the wake region making the body more streamlined. We can use the changes in concavity of the deformation angle data to identify the values of $\tilde{C}a_c$. The value of $\tilde{C}a_c$ is seen to depend on the fiber length as well as the orientation. For the case $\theta_0 = 225^\circ$, $\tilde{C}a_c$ is of $O(1)$ for the 6cm fiber and shifts to $O(10)$ for the 2cm and 4cm cases. For the remaining angles the 6cm fiber displays no yield stress while $\tilde{C}a_c$ for the 4cm and 2cm fibers show an order of magnitude reduction. The shorter fibers in the experiments, namely 2cm and 4cm, display time dependent fluttering at the highest velocity considered here but the 6cm fiber achieves the time dependent flapping at much lower values of $\tilde{C}a_c^{(2)}$ than the other cases. It must be however noted that unsteady motion referred to here was not the

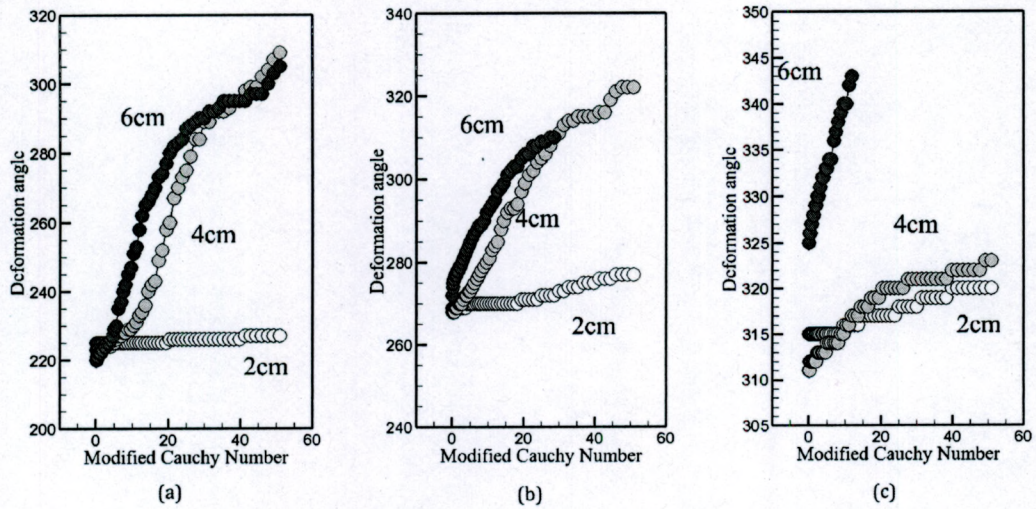


Figure 2.3: These graphs show the average bending of the fibers between their suspension point and free end based on experimental investigations. Variations of the bending with $\tilde{C}a$, fiber length and initial orientation are examined. Panel (a) corresponds to $\theta_0 = 225^\circ$, (b) to $\theta_0 = 270^\circ$, (c) to $\theta_0 = 315^\circ$.

consistent large periodic oscillation of the type observed by.²⁴

Visualizations of the flow structure past the body indicates a complex wake vortex pattern even at fairly low velocities (figure 2.6). The resulting pressure differences between the fore and aft regions of the fiber eventually cause the bending of the fiber as the pressure force exceeds the tension in the fiber. To allow for the visualization past the fiber, we repeated the aforementioned experiments with a thicker fiber. The flow was seeded with microscopic hollow glass spheres of average diameter $13\mu m$ and illuminated using a laser sheet (532nm, 1W laser from Opto Engine LLC). The resulting images of the flow structure via scattering from the seeded particles are shown in figures 2.4 and 2.6.

Visualization of the flow structure along the YZ plane was also conducted in order to discern any significant three dimensional effects. The spherical basal body generates a noticeable dimensional wake; the fiber is however, far too thin to do so. Figure 2.6

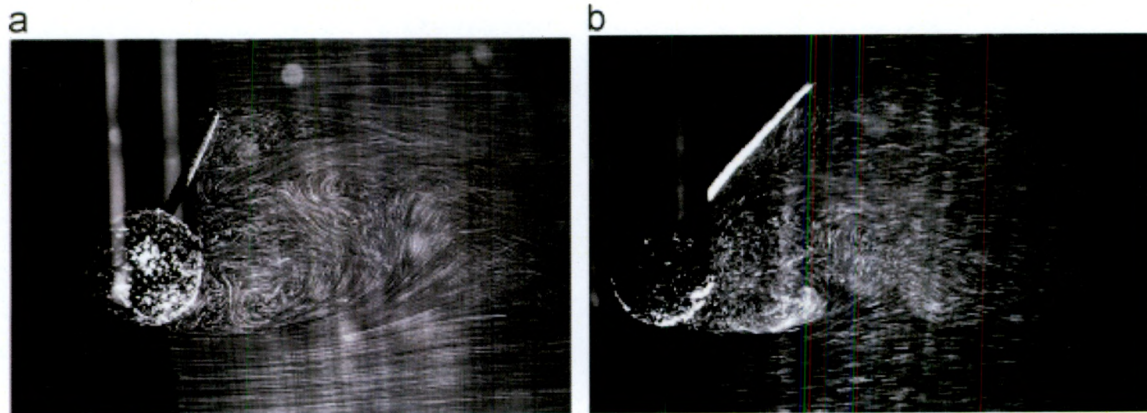


Figure 2.4: Visualization of the wake vortex behind the fiber. Panel (a) shows the vortex structure for a 4 cm fiber at approximately $U=5$ cm/s while panel (b) shows the structure for a 6 cm fiber at a higher velocity of $U=15$ cm/s.

depicts the three dimensional flow structure in the plane Z and is shot from an oblique angle to allow for visual identification of the flow structure. The fiber used for purposes of visualization are thicker (3mm width) than the nylon fibers referred to earlier since the flow past the nylon fibers are practically impossible to visualize due to their slenderness. The red box in figure 2.6 highlights the three dimensional structure which can be seen to be obvious behind the sphere but not as prominent behind the fiber and remains sufficiently small for the flow speeds examined in this study.

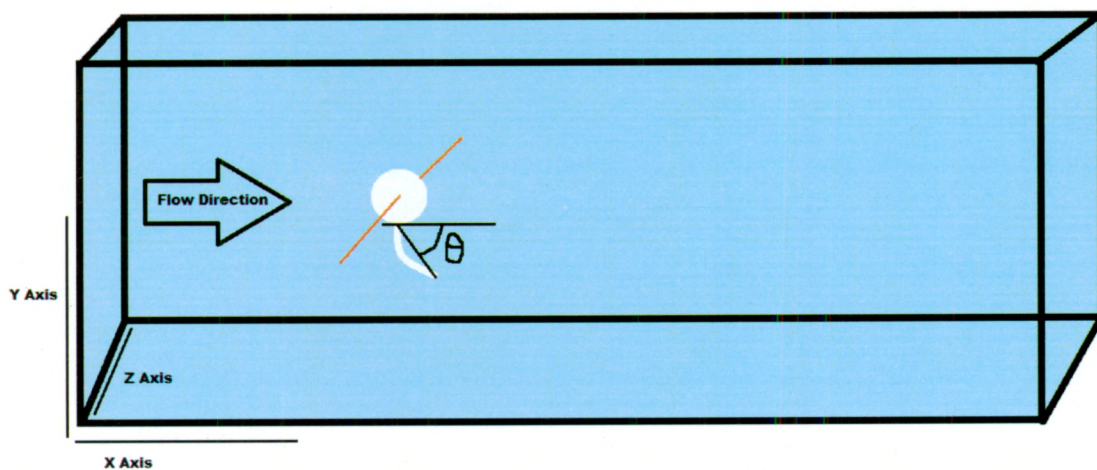


Figure 2.5: An artistic representation of the flow tank showing the x , y , and z axes, along with the direction of the flow, and how θ was measured.

Also, it is reasonable to assume that the symmetry of the flow around the fiber cancels any bending forces along the YZ plane; the flow asymmetry in the XY plane, along which the fiber lies is the only cause of the bending which occurs in the same plane. As a consequence of these observations our following analysis are conducted in two dimensions. Also, while we were unable to measure the drag and lift forces experimentally, they have been studied numerically and discussed in the following section. Close comparisons with experimentally observable parameters are also made to estimate deviations of theoretical results from experiments.

While, the three dimensional computation remains a considerable challenge at this stage in terms of its computational cost and time, large strides have been made. We are currently starting to look at the problem in three dimensions. These preliminary computations appear to confirm our assumptions about the validity of the two dimensional simulations. However, due to the difficulty and computational cost, three dimensional simulations are still impractical for investigations on this scale.

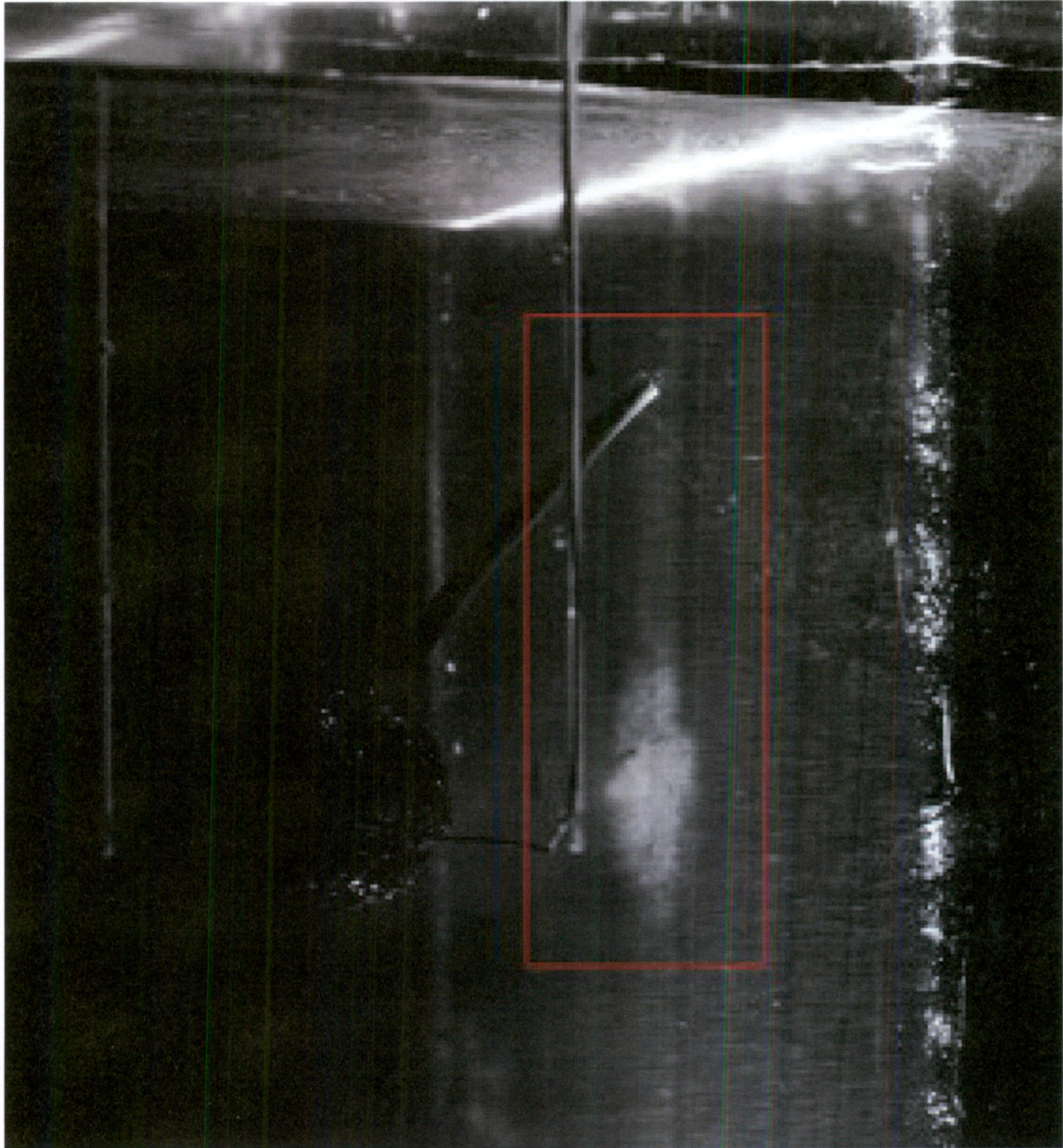


Figure 2.6: The image shows the wake vortex behind the obstacle in the Z direction. The fiber used here is 6 cm in length and the corresponding flow velocity is nearly 15 cm/s. The picture in the red box shows the three dimensionality of the wake flow field. The fuzzy circular region behind the sphere corresponds to the 3d wake structure behind the sphere; the fiber however does not generate any noticeable wake in the third dimension.

Chapter 3

Governing Equations

The numerical simulations were performed using the computer program COMSOL Multi-physics. The simulations were set up using the Fluid Structure Interaction (FSI) module within COMSOL Multi-physics.

The overall attempt was to simulate the bending of an elastic fiber attached to an ellipsoidal basal body. The resolution of this fluid-structure problem followed from solving the following coupled equations:

$$\rho \left(\frac{\partial \mathbf{u}}{\partial t} + \mathbf{u} \cdot \nabla \mathbf{u} \right) - \mu \nabla \cdot (\nabla \mathbf{u} + \nabla^T \mathbf{u}) + \nabla p = \mathbf{F} \quad (3.1)$$

$$\nabla \cdot \mathbf{u} = 0 \quad (3.2)$$

$$\rho \frac{\partial^2 \mathbf{u}_s}{\partial t^2} - \nabla \cdot \boldsymbol{\sigma} = \mathbf{F}_v \quad (3.3)$$

where \mathbf{u} is the incompressible fluid velocity field, \mathbf{u}_s is the displacement of the solid fiber, t is time, μ is the dynamic viscosity, \mathbf{F} is the body force on the fluid, in this case gravitational acceleration times ρ , and \mathbf{F}_v is the force per unit volume on the fiber. The Cauchy stress

tensor for the solid material, σ , is given by²⁶

$$\sigma = \frac{1}{\det(\mathbf{F}_s)} \mathbf{F}_s \mathbf{S} \mathbf{F}_s^T \quad (3.4)$$

where $\mathbf{F}_s = (\mathbf{I} + \nabla \mathbf{u}_s)$, $\mathbf{S} = \mathbf{S}_0 + \mathbf{C} : (\boldsymbol{\varepsilon} - \boldsymbol{\varepsilon}_0)$ and $\boldsymbol{\varepsilon} = \frac{1}{2} (\nabla \mathbf{u}_s + \nabla \mathbf{u}_s^T)$. Here \mathbf{C} , \mathbf{S} , \mathbf{S}_0 , $\boldsymbol{\varepsilon}$ and $\boldsymbol{\varepsilon}_0$ stand for the stiffness tensor, stress tensor, initial stress tensor, strain tensor and initial strain tensor, respectively. In the special case of a homogeneous isotropic media, like that considered in our study, σ reduces to the simple form

$$\sigma_{ij} = K \delta_{ij} \varepsilon_{kk} + 2\mu_s \left(\varepsilon_{ij} - \frac{1}{3} \delta_{ij} \varepsilon_{kk} \right) \quad (3.5)$$

where K is the bulk modulus and μ_s is the shear modulus of the material.

On the solid boundaries of the channel, no-slip conditions are imposed. On the deformable body, the flow velocities are taken to be equal to the rate of deformation of the fiber (i.e. the time rate of change of the displacement).

The FSI module solves the Navier-Stokes equations for the flow in a continuously deforming geometry using the *arbitrary Lagrangian-Eulerian* (ALE) technique. The deformation of the mesh relative to the initial shape of the domain was computed using *hyperelastic smoothing*. Inside the fiber, the moving mesh follows the deformations of the fiber and at the exterior boundaries of the flow domain the deformation was set to zero in all directions. We solved for the time dependent variables using the PARDISO solver (included in Comsol) which was run for 5 seconds. Once the flow field was computed, the net drag and lift forces on the fibers as a function of the flow velocity was evaluated:

$$F_D = \hat{\mathbf{u}}_{\parallel} \cdot \oint_S \mathbf{T} \cdot \mathbf{n} \, dS, \quad (3.6)$$

$$F_L = \hat{\mathbf{u}}_{\perp} \cdot \oint_S \mathbf{T} \cdot \mathbf{n} \, dS, \quad (3.7)$$

where $\hat{\mathbf{u}}_{\parallel}$ is the unit vector in the direction of the fluid flow, $\hat{\mathbf{u}}_{\perp}$ is the unit vector in the direction perpendicular to the fluid flow, S is the surface of the obstacle, \mathbf{T} is the Newtonian stress tensor, and \mathbf{n} is the normal unit vector pointing into the body. Parameters used for the studies are shown in appendices A and B.

Chapter 4

Numerics: Single Fiber Equilibrium Configuration

At the conclusion of the experimental section above, figure 2.6 indicated negligible three dimensional flow around the fiber. This is not to say that there is no three dimensional flow behind the fiber or that the fiber remains unaffected by the flow induced by the basal body. These observations were used to restrict the computational investigations to two dimensions. The three dimensional simulation is extremely challenging and is still in the early stages of testing. This section discusses the relative merit of the numerical method employed to simulate and qualitatively replicate the experimental results. This is done by comparing the numerical estimates of the average bending versus $\tilde{C}a$ with those obtained from experiments (see figure 2.3).

4.1 Set Up

These simulations were conducted inside a two dimensional channel that was 50 cm long and 18 cm high. The front wall was set to be the channel inlet and the back wall was set to be the channel outlet. At the channel inlet the flow is taken to be fully developed and parabolic, while at the channel outlet zero pressure conditions are imposed. The top and bottom walls of the channel were set to have a no slip boundary condition.

The ellipsoidal body inside the channel was centered at the point $x=9$ cm, $y=9$ cm. The semi-major axis was parallel to the direction of the flow, and the semi-minor axis was perpendicular to the direction of the flow. Only the 0.00 eccentricity ellipsoid was studied in the single fiber investigations. The radius of the ellipsoid was 1.25 cm.

The fibers were attached to the ellipsoidal body in three different ways. In the first case, the fiber was oriented at an angle of 90° (270°). In the second case, the fiber was oriented at an angle of 45° (315°). In the third case, the fiber was oriented at an angle of 135° (225°). All angles are with respect to the direction of the flow. In all the cases the fibers were attached to the center of the ellipsoid. Three different fiber lengths were investigated. In the first case the fiber was 2 cm long. In the second case the fiber was 4 cm long. In the third case the fiber was 6 cm long.

A *fine* user controlled mesh was chosen specifically to be calibrated for fluid dynamics problems (see figure 4.1).

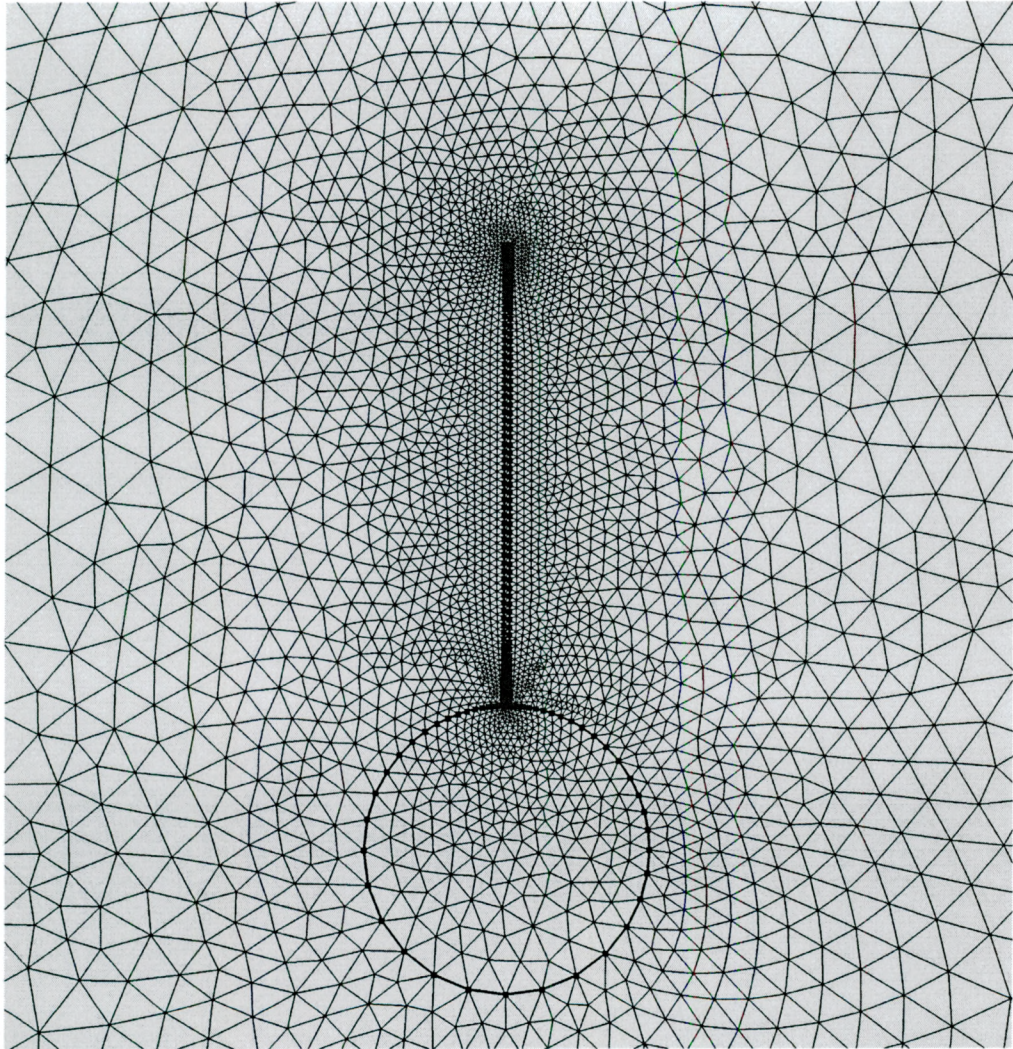


Figure 4.1: The two-dimensional user controlled mesh generated for the fluid structure problem under investigation

4.2 Convergence tests

Several tests were performed to confirm the validity of the computational results. In particular, the effect of mesh density was investigated by computing the steady state drag and lift forces for various mesh density options, as shown in figure 4.2. The x axis denotes the various mesh configurations, where 1 is defined as a 'user controlled mesh'(11381 elements), 2 as 'coarser'(2212 elements), 3 as 'coarse'(3590 elements), 4

as 'normal'(5241 elements), 5 as 'fine'(8609 elements), 6 as 'finer'(16768 elements), 7 as 'extra fine'(37456 elements) and 8 as 'extremely fine'(66682 elements). Numerical convergence was achieved (figure 4.2) and the result seem stable beyond the choice of *normal* mesh. Mesh 1 was the user controlled while meshes 2-8 were automatically generated by Comsol. Based on these estimates the 'fine mesh' or higher was chosen to run all our cases, with grid points ranging between about 9000-12000.

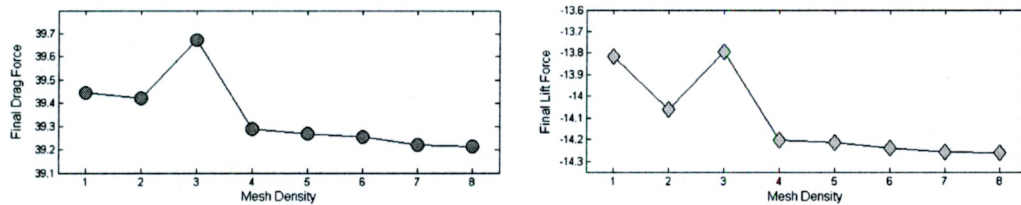


Figure 4.2: The values for drag and lift are computed for a 4 cm fiber of thickness 0.05 cm with an initial orientation of $\theta_0 = 270^\circ$ relative to the flow as a function of different mesh densities. Here the x-axis denotes the various mesh configurations, where 1 is defined as a user controlled mesh, 2 as 'coarser', 3 as 'coarse', 4 as 'normal', 5 as 'fine', 6 as 'finer', 7 as 'extra fine', and 8 as 'extremely fine'.

The computational domain was chosen to match with experimental configuration, apart from the restriction in dimensionality. For this reason the majority of the computational results reported here correspond to the case of $h = 18\text{cm}$. Variations in the values of terminal drag and lift forces for increasing channel heights (in centimeters) were computed and are depicted in figure 4.3 for the sample case of a 4cm fiber at initial angle $\theta = 270^\circ$. Increasing channel heights naturally changes the drag and lift forces which appear to converge to a fixed value. There is a change of nearly 20% in the drag force and about 25% in the lift force as one moves from $h = 18\text{cm}$ to the final channel height of $h = 75\text{cm}$ considered here. It needs to be kept in mind that the convergence of the computed quantities with respect to h is not in question here; the choice of h is dictated by experimental considerations.

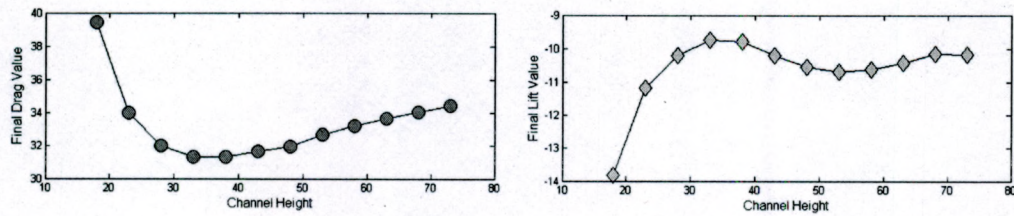


Figure 4.3: The values for drag and lift are computed for a 4 cm fiber with initial an orientation of $\theta_0 = 270^\circ$ relative to the flow, as a function of different channel widths.

4.3 Results: comparison with experiments

A time sequence of the results of our simulations are shown in figure 4.4 for the same cases explored in experiments. The simulations permit us to visualize the evolution of the two dimensional vortex structures and its interaction with the bending of the fiber. As anticipated, the wake structure and resulting pressure differential in the fore and aft regions of the fiber appears to be the driving factor causing the fiber to reconfigure. While the fiber orients into the flow, the primary cause of the first vortex is the fiber. In the streamlined position, it is the sphere which affects the primary vortex (see also figure 2.6) the most while with the fiber in the vertical orientation, the ball and fiber, both contribute equally to the primary vortex.

Figure 4.5 examines the average bending behavior versus $\tilde{C}a$ where the same range in $\tilde{C}a$ has been maintained as in experiments. The numerical results are in good qualitative agreement with experiments and show the same overall profiles observed in figure 2.3. Specifically, we note that the average deformation angle increases sharply with the length of the fiber, i.e. longer fibers are more prone to bending than the shorter ones. The 2cm fiber displays little propensity to bend, much like in experiments. In terms of orientation, the deformation angle is largest when the fiber protrudes into the flow direction and least when the fiber is in a more streamlined configuration (see also figure 4.6(d)). This is not

so obvious for the 6cm fiber which shows a drop in the average bending past $\tilde{C}a \approx 40$ which is caused by the free tip of the fiber dropping below its maximum height in this orientation. While the 4cm and 6cm fibers show no critical behavior (i.e. absence of $\tilde{C}a_c$), the 2cm fiber exhibits critical behavior at $O(10)$ for the streamlined case and at $O(1)$ for the remaining two orientations. In these cases, the deviations from experimental observations can be attributed primarily to the mismatch of material properties of the fibers which had to be approximated in experiments. We also considered the case when the diameter of the basal body is reduced from 2.5cm to 0.06cm (note the triangular points in figure 4.5), in order to understand the impact of the body size on the fiber deformation. Our preliminary calculations revealed that the diameter of the basal body does indeed make a noticeable difference when the fiber protrudes into the flow but is less so when the fiber is in a streamlined position.

The x -axis in figure 4.5 was chosen to conform with the experimental range. In this range, no time dependent motion was observed for any of the fibers. However, we extended our study to explore values of $\tilde{C}a_c^{(2)}$ for the 2cm and 4cm fibers (the 6cm fibers broke down in the unsteady regime), each oriented at three different configurations. These simulations also display sensitivity to the orientation of the fiber. At certain critical flow speeds the fibers transition from steady state to periodic oscillations, which are not actually observed in our experiments, in the range of flow speeds considered. Table 1 denotes the critical speeds which triggers the onset of oscillations. As in experiments, the larger fibers transition out of equilibrium more easily than the smaller ones. However, unlike in experiments, the simulations indicate that fibers oriented at $\theta_0 = 225^\circ$ oscillate at lower flow speeds than the $\theta_0 = 315^\circ$. This apparent discrepancy can be attributed to lack of a sufficient range of speeds in the observations, non-constant stiffness across the fiber and three dimensional effects.

Critical Speeds	225°	270°	315°
2cm	75.08 cm/s	42.63 cm/s	305.18 cm/s
4cm	39.68 cm/s	54.43 cm/s	83.93 cm/s

Table 4.1: Critical flow speeds at which the fibers display periodic oscillations.

Yet another way to classify the effect of the flow upon the bending configurations of the fiber is by examining the overall drag on the system. It is well known that for rigid bodies the drag force varies as the square of the velocity.⁴ However for flexible bodies, since the bodies can bend to reduce drag, the relation is markedly different from the rigid body case and can be given by $F_D \propto U^\alpha$ ²⁹ where, the exponent, $1 < \alpha < 2$. Several studies performed on flexible bodies of different shapes and materials seem to put the exponent in the range 1-1.5.^{1,12,29} It is to be noted that in these studies the body is always initially held perpendicular to the flow direction. The results of our calculation of the drag exponent are indicated in the table 2. A least squares fit to the drag force values applied to the results of our two dimensional numerical computations (see figure 4.6) yield the values of α which seem to conform to the previously reported ranges. The exponents are seen to be sensitive to the orientation and length of the fiber although it is not quite clear if there is any distinct pattern. It has been observed¹² that there is a critical length below which the drag shows an increasing trend and above which the drag decreases with increasing length. While no such trend is seen here, it is plausible that such a reversal also shows itself as we combine the fiber length with its orientation. The values obtained in our computations clearly correspond to the case of small deformations¹² *Table 1*; after all the velocities considered in our study are well below 1ms^{-1} .

Drag Exponent	315°	270°	225°
2cm	1.19	1.24	1.22
4cm	1.19	1.26	1.29
6cm	1.14	1.28	1.40
4cm (small sphere)	1.20	1.33	1.30

Table 4.2: The drag exponents for fibers of varying lengths and orientations based on least squares fit of our 2D simulations.

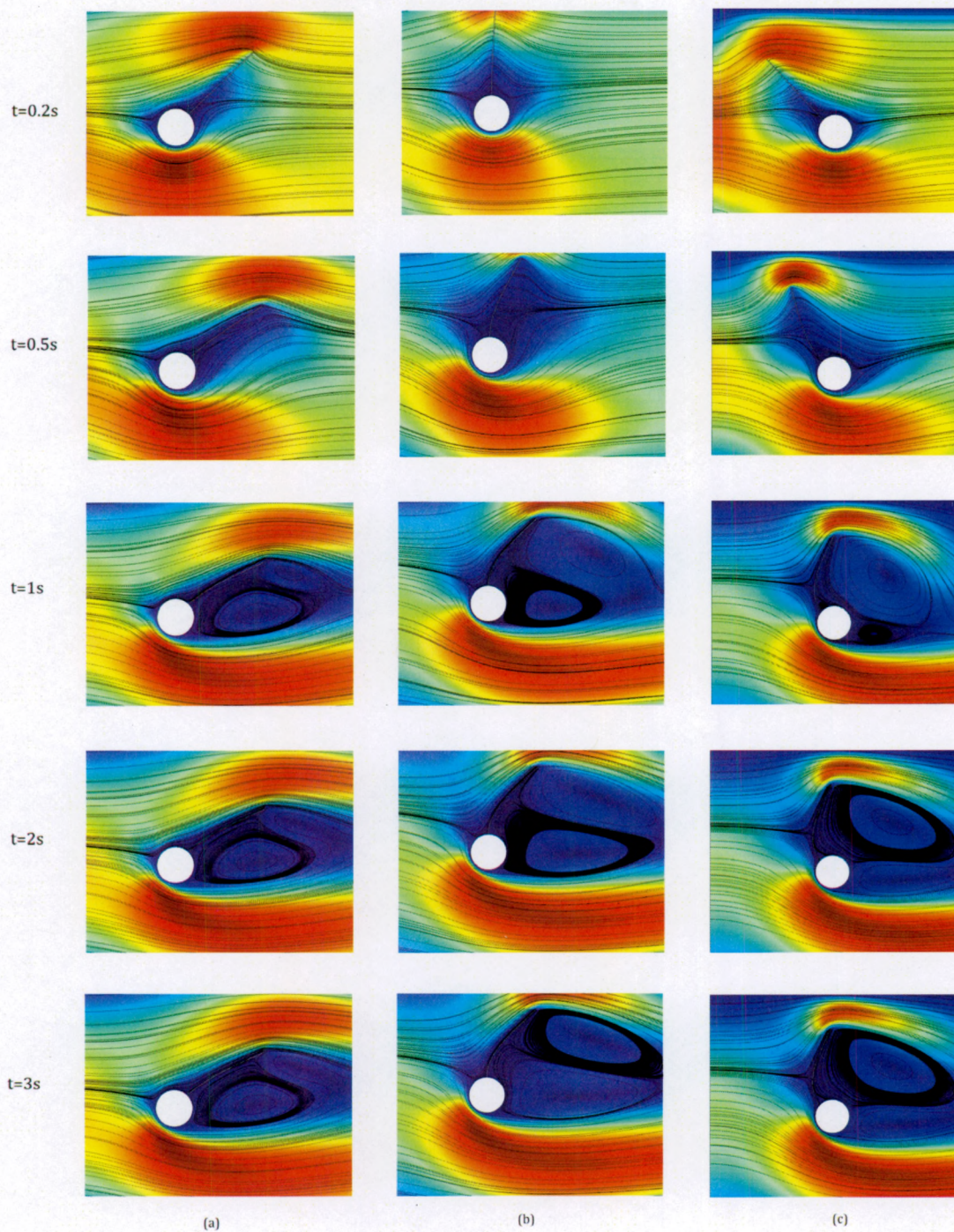


Figure 4.4: The time evolution of a 4 cm fiber at various orientations are depicted along with the corresponding flow structure. The fibers achieve their steady configurations as the flow simultaneously evolves into its steady state. The wake vortex structure is also seen to depend on the fiber orientation.

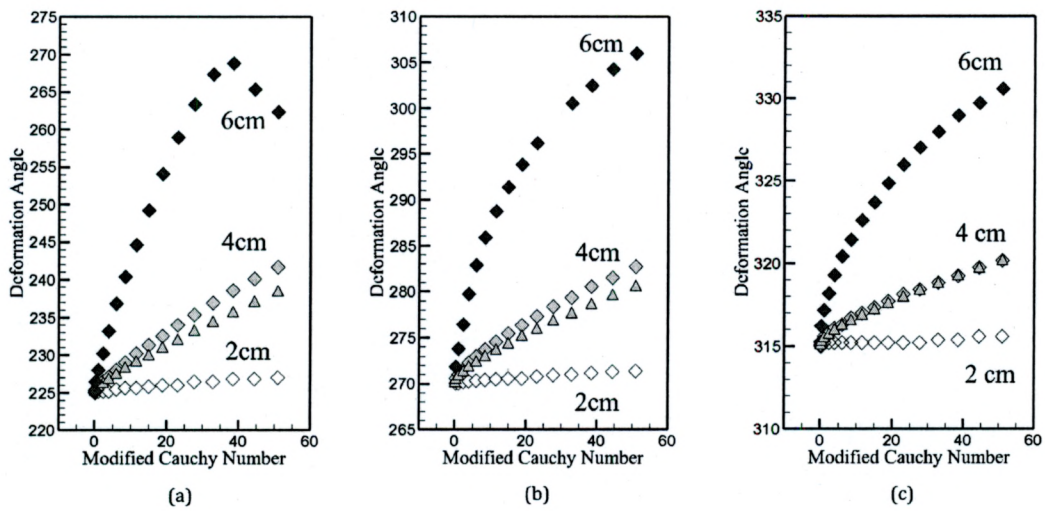


Figure 4.5: These graphs show the average bending of the fibers, between their suspension point and free end, versus $\tilde{C}a$ for three different fiber lengths and initial orientations, based on the 2d numerical simulations. The triangular points refer to the 4cm case where the body was reduced in size. Panel (a) corresponds to $\theta_0 = 225^\circ$, (b) to $\theta_0 = 270^\circ$, (c) to $\theta_0 = 315^\circ$

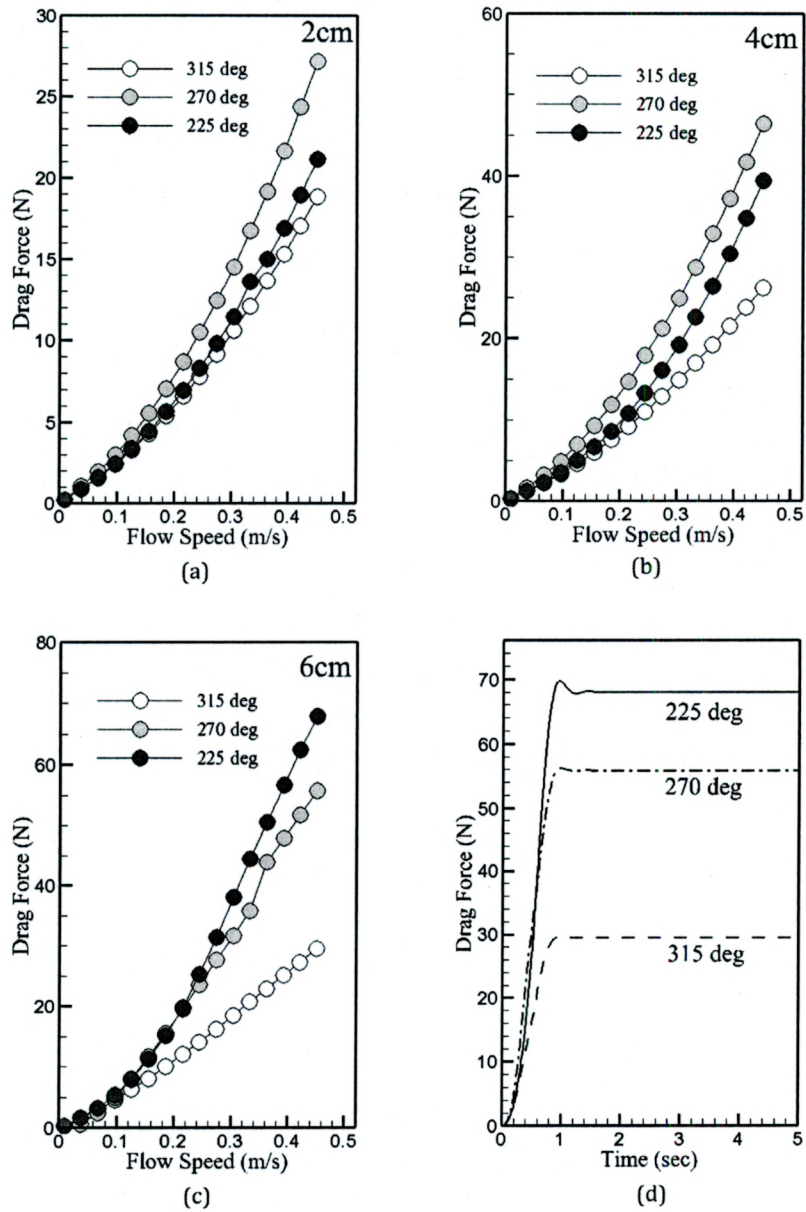


Figure 4.6: The panels (a), (b), and (c) show variations in drag versus U . Panel (d) shows the drag transition of a sample case, the 4 cm fiber at $\theta = 270^\circ$. In all cases here, the fiber is seen to reach steady state at about 1 s with the highest drag when the fiber protrudes into the flow and the least drag when the fiber is in its most streamlined configuration.

Chapter 5

Numerics: Optimal Body Shape with Two Fibers

The previous section demonstrated that we could qualitatively model physical phenomena using two dimensional numerical simulations. After that success it was decided that we should broaden our investigations to a body with two fibers. This is because a basal body with a single fiber is rarely found in the natural world. For example, birds do not have a single wing and fish do not have a single fin. Thus a body with two fibers is a more realistic representation of the structures found in the physical world. In this section we will investigate an eccentric ellipsoid with two fibers. We will look at how drag and bending change as the orientation of the fibers, and the eccentricity of the body changes. We also look at the effects of computational parameters such as mesh density and channel height.

5.1 Set up

These simulations were conducted inside a two dimensional channel that was 50 cm long and 18 cm high. The front wall was set to be the channel inlet and the back wall was set to be the channel outlet. At the channel inlet the flow is taken to be fully developed and parabolic, while at the channel outlet zero pressure conditions are imposed. The top and bottom walls of the channel were set to have a no slip boundary condition.

The ellipsoidal body inside the channel was centered at the point $x=9$ cm, $y=9$ cm. The semi-major axis was parallel to the direction of the flow, while the semi-minor axis was perpendicular to the direction of the flow. Three different eccentricities were used for the ellipsoidal body, 0.00, 0.50, and 0.99. In all three cases the area of the ellipse was conserved. The area of the ellipse was based on the 0.00 eccentricity case, which had a radius of 1.25 cm. The dimensions of the ellipsoidal bodies can be found in table 5.1.

Eccentricity	Semi-Major Radius (cm)	Semi-Minor Radius (cm)
0.00	1.25	1.25
0.50	1.34	1.16
0.99	3.33	0.47

Table 5.1: The dimensions of the ellipsoidal bodies used, in centimeters.

As mentioned earlier, in this study two fibers were used. These fibers were attached to the ellipsoidal body with three different orientations. In first and second cases, the fibers were attached to the center of the body. In the first case the top fiber was oriented at an angle of 90° and the bottom fiber at an angle of 270° . In the second case the top fiber was oriented at an angle of 45° and the bottom fiber at an angle of 315° . In the third case, the fibers were affixed to the edge of the body along the semi-minor axis. The top fiber was oriented at an angle of 45° and the bottom fiber at an angle of 315° . This third case was done in order to create a more streamlined object, an object whose fibers both were

swept back and free from wake effects. All angles are with respect to the direction of the flow. Visualizations of the different models used can be found in figure 5.4, as well as, in appendix C.

In the first and the second cases the fibers, attached at the center of the body, had a length of 4 cm. In the third case the length of the fiber was reduced in order to compensate for the fiber being fixed along the edge. This was necessary to ensure that the fiber in the third case did not protrude further from the body than the fibers in the first and second cases. The following equation was used to determine the length of the fibers in the third case,

$$\text{Fiber Length} = 4 - \text{Semi-Minor Radius}. \quad (5.1)$$

Due to the availability of better computing hardware, this study used the physics based mesh that is built into COMSOL, rather than the user controlled mesh which had been used in the equilibrium configuration study. The physics based mesh was chosen in order to reduce the numerical error in the simulations. This in no way invalidates the previous study, which was qualitatively similar to the physical experiments that were performed. This was merely an attempt to tighten up the numerical results and reduce any errors. The mesh density was set to "Fine" and consisted of 87,277 elements.

5.2 Biological Models

For the biological comparison two sets of two dimensional models were created in COMSOL Multi-physics based on biological organisms. The data for these models

came from *Determination of Body Density for Twelve Bird Species*, by Hamershock et al.¹³ In order to determine the densities of the twelve bird species, careful measurements were taken of, among other factors, the length, circumference, and wingspan of twelve specimens from each of the twelve species.¹³ These measurements were then averaged out to give a mean length, circumference, and wingspan for each of the twelve species measure.¹³ Note that we are not trying to model birds, just bird like shapes. Bird like shapes were chosen due to a lack of readily available data on the bodily dimensions of other types biological organisms.

In the first set of biological models, three different organisms were modeled using the data from Hamershock et al. These organisms were the Herring Gull, the House Sparrow, and the Canadian Goose. All three fiber orientations were investigated in this set of models. The fiber lengths were maintained at 4cm. Meanwhile, the eccentricity of the ellipsoidal body was modified to be in agreement with the general shape of the organism's body. For all of the biological models that were created the area of the body was kept the same as the area of the ellipses that had previously been used.

In the second set of biological models, nine different organisms were modeled using the data from Hamershock et al.¹³ As before, the eccentricity of the ellipsoid was modified to be in agreement with the general shape of the organism's body. In this set only the 90° case of fiber orientation was investigated. This orientation was chosen because, often when organisms are gliding in a steady state their appendages are roughly at a 90° orientation. Of course real appendages have joints and are significantly more complicated, however, only a qualitative idea for the forces involved was being sought. Furthermore, the length of the fibers were also modified in this set of models, so as to match length of organism's presented in Hamershock et al.¹³ In all of the biological models that were created the

area of the body was kept the same as the area of the ellipses that had previously been used.

In order to scale the biological models down to fit the computational domain the following equation was used,

$$1.25^2 = S_b^2 \cdot \frac{\text{Organism Length}}{2} \cdot \frac{\text{Organism Circumference}}{2\pi}. \quad (5.2)$$

Where 1.25 was the original radius of the 0.00 eccentricity ellipse and S_b is the scaling factor. The semi-major radius was then became,

$$\text{Semi-Major Radius} = S_b \cdot \frac{\text{Organism Length}}{2}. \quad (5.3)$$

Meanwhile the semi-minor radius became,

$$\text{Semi-Minor Radius} = S_b \cdot \frac{\text{Organism Circumference}}{2\pi}. \quad (5.4)$$

As mentioned before fiber length was altered in the second set of biological models. This was done in order to get a more qualitative idea of the drag forces experienced by the biological models. The fiber length was based on the measurements of the wingspan reported by Hamershock et al.¹³ Like the body measurements, the wingspan measurements were also scaled. In order to scale the wingspan down so as to fit the computational domain, first the ratio between the wingspan and body length was calculated. This was done using the equation,

$$\text{Wingspan} = S_w \cdot \text{Organism Length}. \quad (5.5)$$

Where S_w is the ratio of wingspan to organism length. Then the length of each fiber was set to

$$\text{Fiber Length} = S_w \cdot \text{Semi-Major Radius}. \quad (5.6)$$

The dimensions used for the second set of biological models can be found in Table 5.2.

Model	Semi-Major Radius	Semi-Minor Radius	Fiber Length
D. Chicken	2.78397	0.56125	4.22153
R. Dove	2.98340	0.52373	5.87402
Mallard	3.20940	0.48685	4.55125
H. Sparrow	3.16092	0.49432	4.87487
H. Gull	3.15654	0.49501	7.50682
E. Starling	3.04393	0.51332	5.28086
C. Grackle	3.25777	0.47962	4.77260
C. Goose	3.04477	0.51318	5.39231
B. Cowbird	3.02547	0.51645	5.20394

Table 5.2: Dimensions of the biological models in centimeters.

For the second set of biological models the width of the channel was increased from 18 cm to 50 cm. This was done in order to reduce the effect of the channel wall on the results of the simulations. The length of the channel remained constant at 50 cm, as in the previous simulations.

5.3 Convergence Tests

In order to determine the effect of computational parameters, two convergence tests were performed. The first convergence test was performed to determine what effect the various meshes had on the results of the numerical simulations. The second convergence test was performed to determine what effect the channel height had on the results of the

numerical simulations. In both tests the 0.00 eccentricity ellipsoid with fibers at 90° was used and the mean flow speed was set to 0.451 m/s.

For the mesh convergence test the steady state drag force and deformation angles

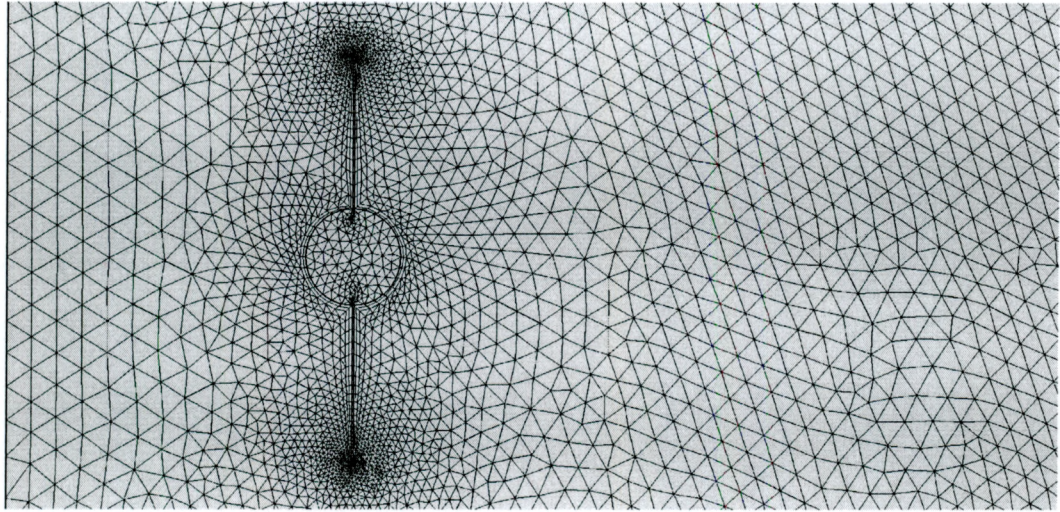


Figure 5.1: The two-dimensional triangular *fine* mesh generated in COMSOL for the fluid structure problem under investigation

were computed using each of the nine mesh density settings. The results of this test can be found in figure 5.2, where drag and deformation angle are shown as a function of mesh density. The density settings checked are, in order from coarsest to finest: 'Extremely Coarse' (10701 elements), 'Extra Coarse' (13883 elements), 'Coarser' (21637 elements), 'Coarse' (36736 elements), 'Normal' (53742 elements), 'Fine' (87277 elements), 'Finer' (160060 elements), 'Extra Fine' (347474 elements), and 'Extremely Fine' (589025 elements). The test cases that used the four coarsest meshes, Extremely Coarse, Extra Coarse, Coarser, and Coarse, failed to compute the entire simulation. The test cases that used the other five meshes successfully completed the computations. The test cases that used the three finest meshes, Extremely Fine, Extra Fine, and Finer, were deemed to take excessively long to compute. The computational times for each mesh setting can be found in table 5.3. All of the mesh density settings, which completed the computations, gave

similar results with no more than a 2% difference between the highest and lowest drag values, and no more than a 4% between the largest and smallest deformation angles.

Mesh Density	Computation Time
Normal	2 min, 52 sec
Fine	4 min, 57 sec
Finer	9 min, 33 sec
Extra Fine	23 min, 38 sec
Extremely Fine	46 min, 45 sec

Table 5.3: Comparison of the time taken to perform each numerical simulation arranged by mesh density.

As in the previous chapter, the computational domain was chosen to match with experimental configurations. Fourteen different channel heights were checked. These heights ranged from 13 cm to 78 cm in 5 cm intervals. The results of this test can be found in figure 5.3, where drag and bending are shown as a function of channel height. This test found that beyond 33 cm the channel height did not play a significant role in bending or drag. However, at the channel height this study was using, 18 cm, the channel's height indeed contributed to the drag force and bending experienced by the ellipsoid fiber system. There was a nearly 69% change in both the drag force and deformation angle as the channel expands from 13 cm to 78 cm, with a smooth convergence beyond 33 cm. It is important to once again keep in mind the the convergence of drag force and deformation angle with respect to h is not in question; h is dictated by experimental considerations.

5.4 Checks for Accuracy

Since there were no physical experiments performed for this study, two checks were performed in order to gauge whether or not the numerical simulations were providing accurate results. First, a series of benchmarking simulations was performed and the results of those simulations were compared to the existing literature. Second, the divergence of the velocity field was checked for each of the numerical simulation that was run.

While the types of numerical simulations that were performed in this study are not new, the types bodies that were investigated have not been previously studied numerically. Because of this there was no data in the existing literature to compare the results of this study to. In order to check that the results of this study were reasonable a series of benchmarking simulations was ran. Previous work with this kind of cylindrical body using COMSOL was performed by Cortes et al.⁷ Cortes et al. ran simulations of a fluid flow past a cylindrical body, with Reynolds numbers between 31.25 and 312.5.⁷ Using the results of their simulations, they calculated the Drag Coefficient of their two dimensional cylindrical body.⁷ They found that their Drag Coefficient was in close agreement with the Drag Coefficient for a cylindrical body in the existing literature.⁷ For our benchmarking simulations we copied the setup that Cortes et al.⁷ used, with the exception of the meshing. Cortes et al. used a different mesh density for each case. Their mesh density ranged from 8474 to 17376 elements.⁷ The mesh that was used for our benchmarking simulations had its density held constant at 6510 elements. It is worth noting at this point that the mesh in our benchmarking simulations only has 6510 elements, whereas in our simulations the mesh has 87,277 elements. This is due to the geometry of the body. In our simulations the mesh becomes finer around the fibers and very fine around the tips of the fibers. This substantially increases the number of elements in the mesh. Meanwhile, in the benchmarking simulations there were no fibers attached to the body.

The results of our benchmarking simulations can be found in table 5.4. The computed Drag Coefficient is the value that was calculated from the results of these benchmarking simulations. Corte's Drag Coefficient is what was reported by Cortes et al. The Literature Drag coefficient is from the existing literature.⁷ The Error vs Lit is the percent error in our computed Drag coefficient versus that found in the literature.

Reynolds Number	Our Computed C_d	Cortes' C_d	Literature C_d	Error vs Lit
31.25	3.726884	2.937875	2.903	28.38%
59.375	2.321026	2.252767	2.258	2.79%
78.125	1.623477	1.609433	1.6129	0.65%
90.6	1.541203	1.551598	1.5564	0.97%
100	1.472457	1.501333	1.5	1.83%
312.5	1.432713	1.4225	1.3225	8.33%

Table 5.4: Results of the benchmarking simulations. The Computed Drag Coefficient is the value that was calculated from the results of these benchmarking simulations. The Cortes' Drag Coefficient is what was reported by Cortes et al. The Literature Drag coefficient is from the existing literature. The Error vs Lit is the percent error in our computed Drag coefficient versus that found in the literature.

In all of the simulations that were ran the divergence of the velocity field, $\nabla \cdot \mathbf{u}$, was checked. Since the fluid flow is incompressible, by conservation of mass, $\nabla \cdot \mathbf{u}$ is supposed to be equal to zero. However, COMSOL uses numerical solvers. For that reason $\nabla \cdot \mathbf{u}$ is unlikely to be exactly zero. Instead $\nabla \cdot \mathbf{u}$ should be a reasonably small number. If $\nabla \cdot \mathbf{u}$ is large, then it is an indication that the simulations are accumulating errors and generating inaccurate results. In all of the simulations that were ran, the largest value for $\nabla \cdot \mathbf{u}$ that was produced was of 6.33×10^{-3} . This value occurred during the benchmarking simulations, when the velocity of the flow was set to 12.5 m/s. During the investigative simulations, with velocities ranging from 0.009 to 0.451 m/s, the divergence was consistently between the orders of 10^{-6} to 10^{-4} . These values were deemed sufficiently small for the purposes of this study.

5.5 Results

These simulations show that ellipsoidal bodies with higher eccentricity experience lower drag forces than bodies with lower eccentricity (figure 5.5). There was a slight reduction in the drag force of 0.50 eccentricity body versus the 0.00 eccentricity body. However, the reduction in the drag force experienced by the 0.99 eccentricity model was considerably greater. This reduction was versus both the 0.00 eccentricity and the 0.50 eccentricity models. In all three of the eccentricities studied, the models with fibers oriented 45° fixed along the edge consistently experienced the lowest drag force. This was followed by the models with fibers oriented at 45° , which experienced a slightly higher drag force. Meanwhile, the models with fibers oriented at 90° experienced the largest drag force, by a considerable margin.

These simulations further show that fibers which are oriented with the flow experience less bending than fibers which are oriented perpendicular to the flow (figure 5.6). This result is in agreement with the findings of the single fiber equilibrium configuration study. There was a slight reduction in the bending between the models with fibers oriented at 45° fixed along the edge versus the models with fibers oriented at 45° . While, the reduction in bending between the models with fibers oriented at 45° , both fixed along the edge and fixed at the center, versus the models with fibers oriented at 45° was considerably larger. It is interesting to note that the reduction in bending was not consistent between all three eccentricities investigated.

In both cases where the fibers were fixed at the center the 0.00 eccentricity models experienced the most bending. This was followed by the 0.50 eccentricity models, which experienced slightly less bending. Finally, the 0.99 eccentricity models experienced the least amount of bending. In the case where the fibers were fixed along the edge this pattern

was reversed. The 0.99 eccentricity model experienced the most bending. Meanwhile the 0.00 eccentricity model experienced the least amount of bending. This reversal of the bending profile likely stems from the how the fiber length for bodies with fibers oriented at 45° fixed along the edge was determined. In equation (5.1) the length of the semi-minor radius is subtracted from the initial length of the fiber. This in turn results in the 0.99 eccentricity model having the longest fibers, which are thus more readily deformed. Note however, that even though the bending profile is reversed, the bodies with fibers oriented at 45° fixed along the edge sustained less bending than did bodies with other fiber orientations. Which is to be expected, since the bodies with fibers oriented at 45° fixed along the edge are more streamlined than the bodies with other fiber orientations.

Taking all of the data together, these simulations reveal that drag was the least for models with high eccentricity and fibers positioned with the fluid flow (figure 5.7). In particular the 0.99 eccentricity model with fibers oriented at 45° from the edge experienced the lowest drag force. From there the drag force increased in every case, with the 0.00 eccentricity model with fibers oriented at 90° experiencing the greatest drag forces. These findings make intuitive sense, as more streamlined systems are expected to experience less drag than less streamlined systems.

The reduction in drag force was most strongly associated with the orientation of the fiber. All of the models with fibers oriented at 45° , both fixed along the edge and fixed at the center, experienced significantly less drag than the models with fibers oriented at 90° . The eccentricity of the model was also associated with a reduction in drag force, though not as strongly as fiber orientation. The higher eccentricity models consistently experienced lower drag forces than the lower eccentricity models. Both of these findings are consistent with earlier observations.

Three biological models were also investigated and compared to this data. The biological models were all highly eccentric ellipsoids with eccentricities between 0.97 and 0.99. Even at these high eccentricities, more highly eccentric models experienced lower drag forces compared to their slightly less eccentric counterparts (figure 5.8).

Drag, or Vogel, exponents were also calculated and found to be in agreement with the existing literature. They ranged from a high of 1.271 to a low of 1.158. The highest was observed in the 0.50 eccentricity case with fibers oriented at 90°. The lowest was observed in the 0.00 eccentricity case with fibers oriented at 45°. The observed Vogel exponents for each eccentricity and orientation can be found in table 5.5.

	0.00 Eccentricity	0.50 Eccentricity	0.99 Eccentricity
45° from the edge	1.209	1.206	1.170
45°	1.158	1.162	1.162
90°	1.269	1.271	1.270

Table 5.5: The drag exponents for bodies of varying eccentricities and fiber orientations based on least squares fit of our 2D simulations.

5.6 Biologically Relevant Results

The biological results are slightly more complicated (figure 5.11). In contrast to the other investigations of this study, the length of the fiber was varied in these investigations. This revealed that in general, drag force does decrease with higher eccentricity (figure 5.9). However, there was a much stronger correlation between fiber length and drag force (figure 5.10). While in not every case the more eccentric bodies were subjected to a lower drag force, usually a higher eccentricity amounted to lower drag. By comparison, in each and every case that was investigated, the models with shorter fibers experienced a lower

drag force compared to the models with longer fibers.

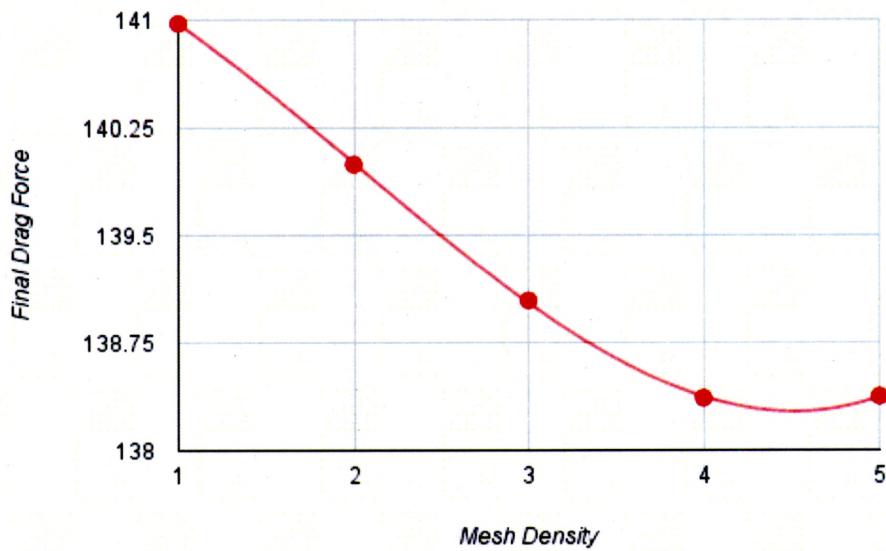
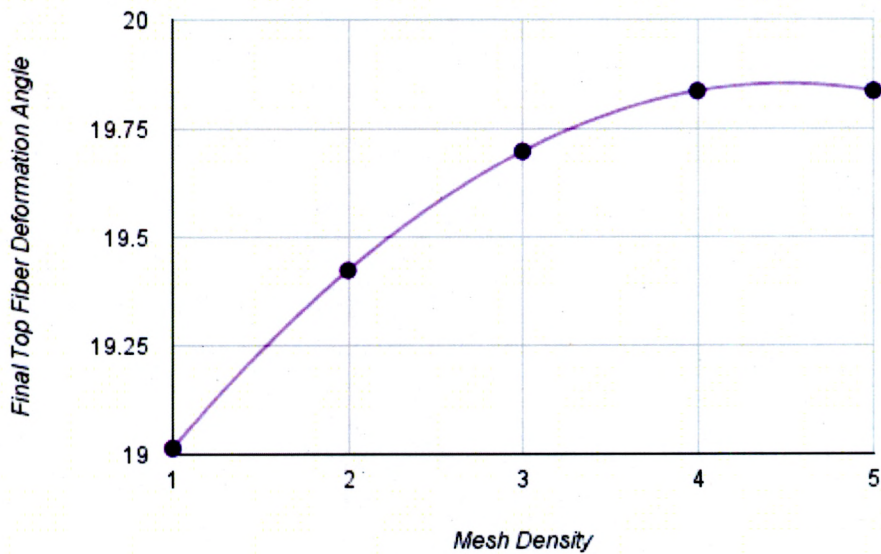


Figure 5.2: Results of Mesh Convergence Study: drag force and deformation angle as functions of mesh density.

1 = 'Normal', 2 = 'Fine', 3 = 'Finer', 4 = 'Extra Fine', 5 = 'Extremely Fine'.

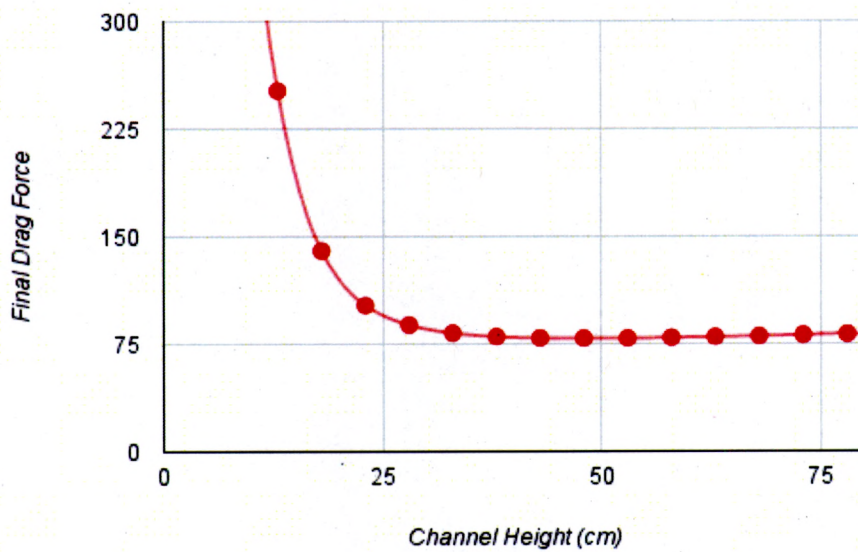
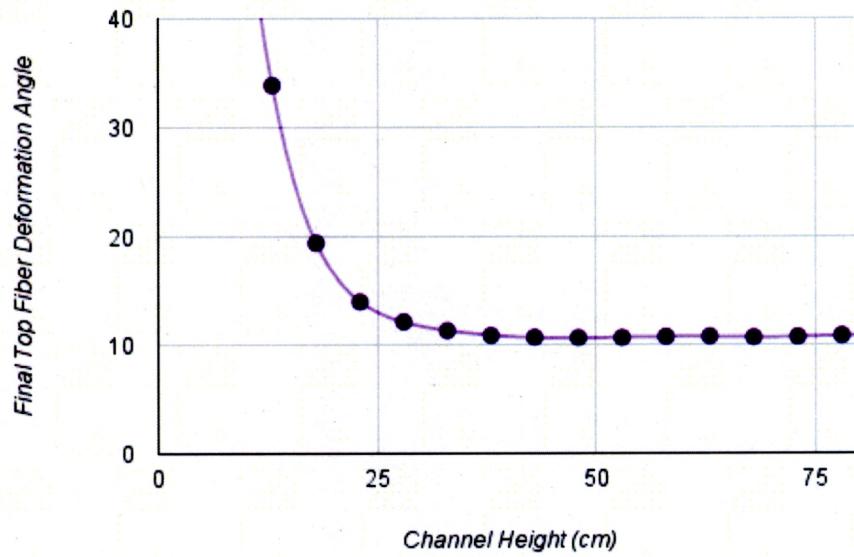


Figure 5.3: Results of Channel Height Convergence Study: drag force and deformation angle as functions of channel height. Channel height given in centimeters.

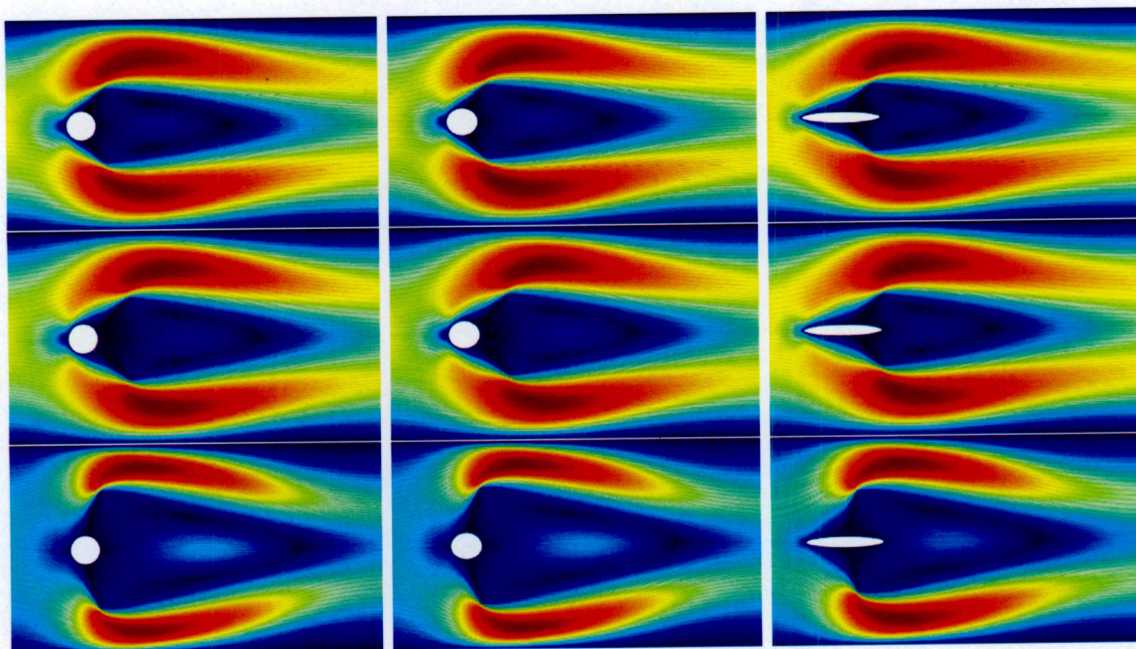


Figure 5.4: Models in steady state configuration

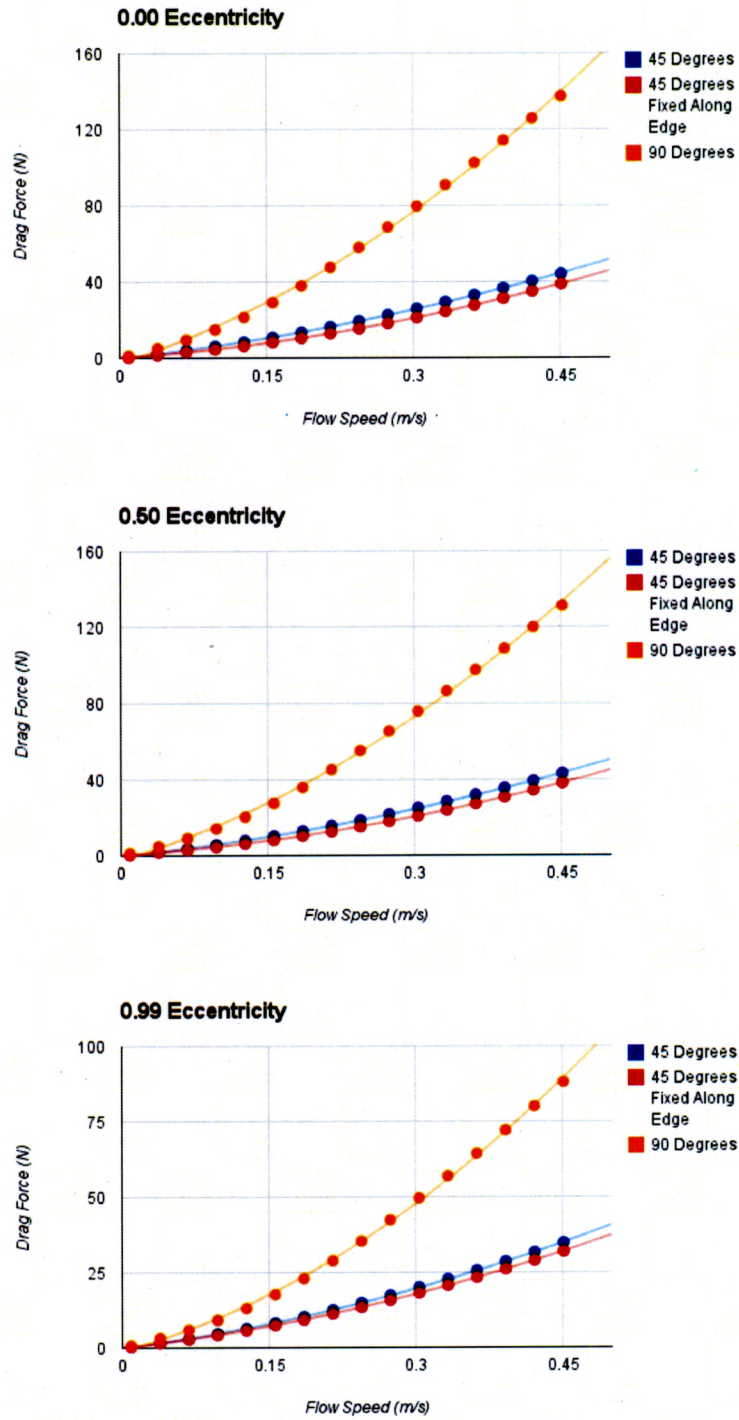


Figure 5.5: Velocity Versus Drag, by Eccentricity

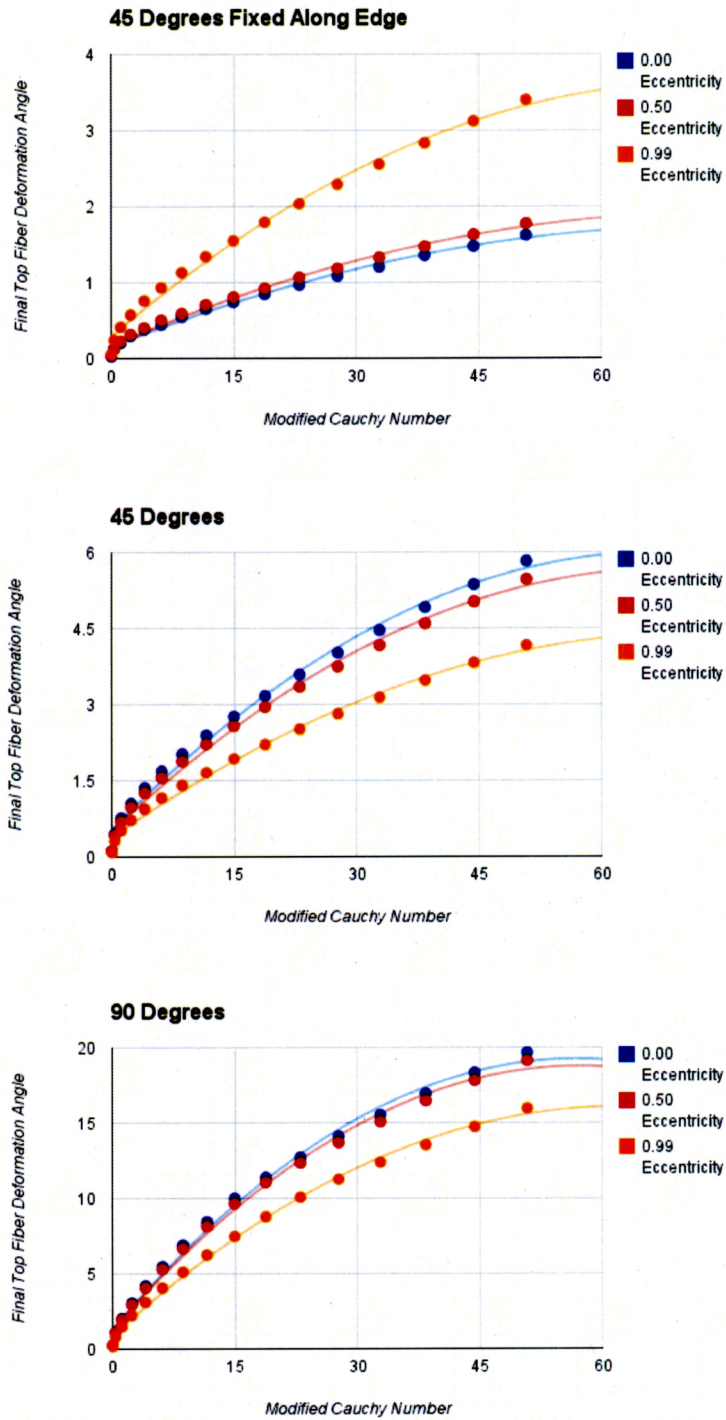


Figure 5.6: Modified Cauchy Number Versus Bending, by Fiber Orientation

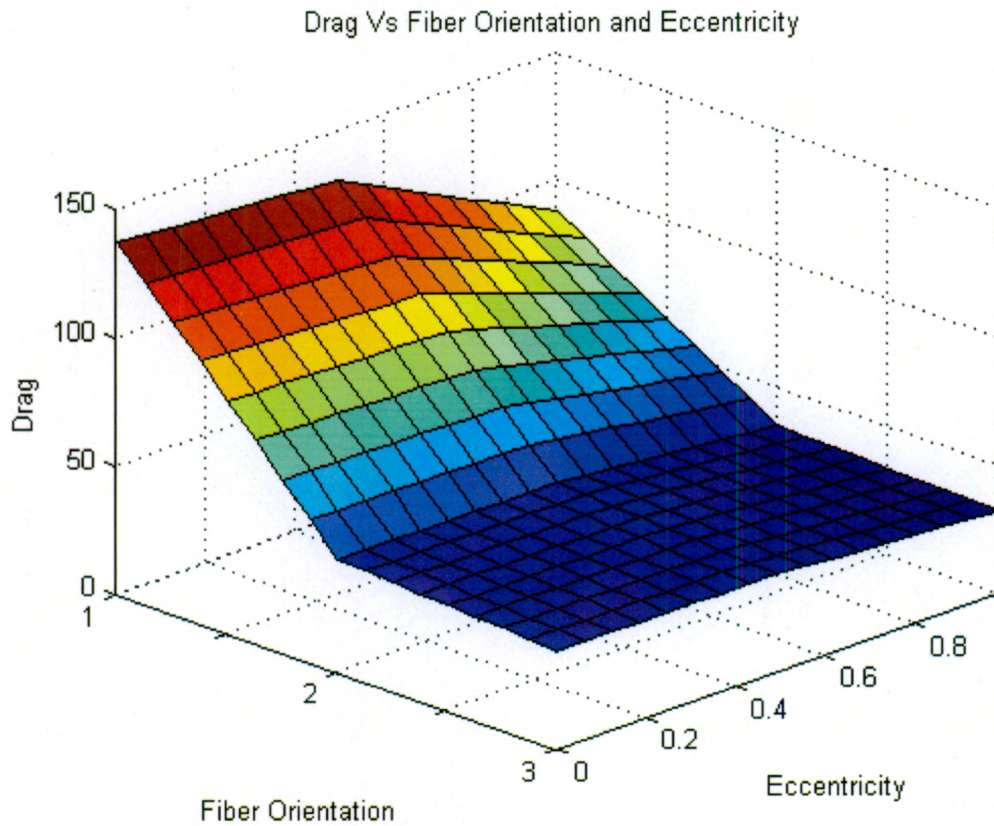


Figure 5.7: Drag Versus Fiber Orientation and Eccentricity. This graph shows that the drag force the ellipsoid-fiber system experiences is more strongly associated with the orientation of the fibers than the eccentricity of the body. Orientation 1: 90° , Orientation 2: 45° , Orientation 3: 45° fixed along the edge

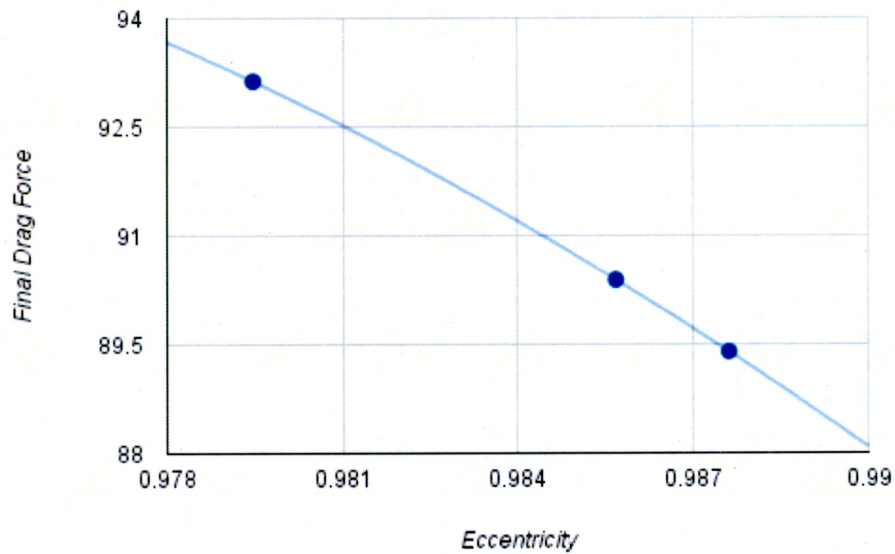


Figure 5.8: Drag Versus Organism Eccentricity

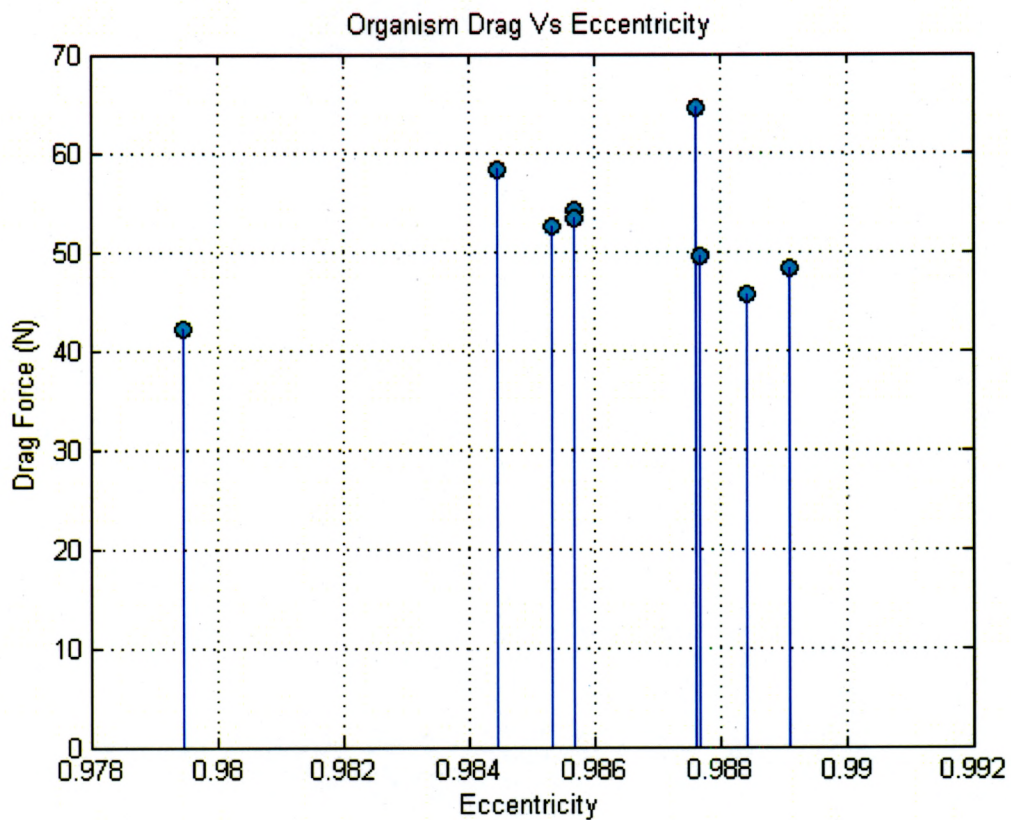


Figure 5.9: Biological Model: Eccentricity vs Drag Force

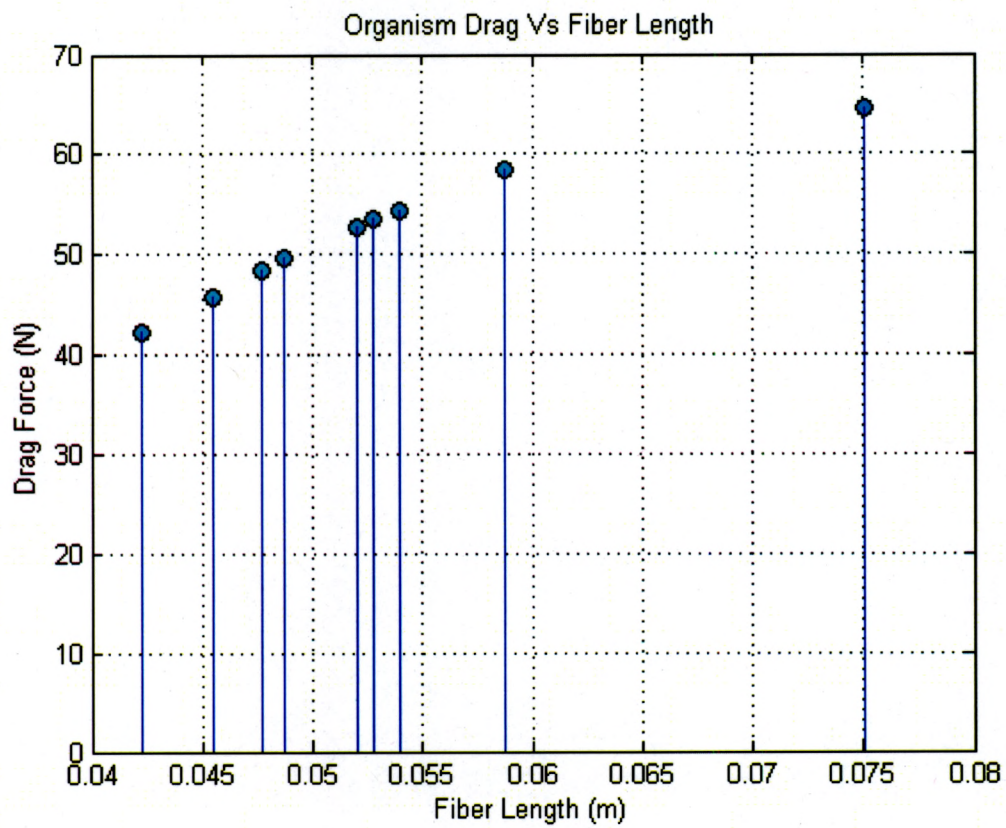


Figure 5.10: Biological Model: Fiber Length vs Drag Force

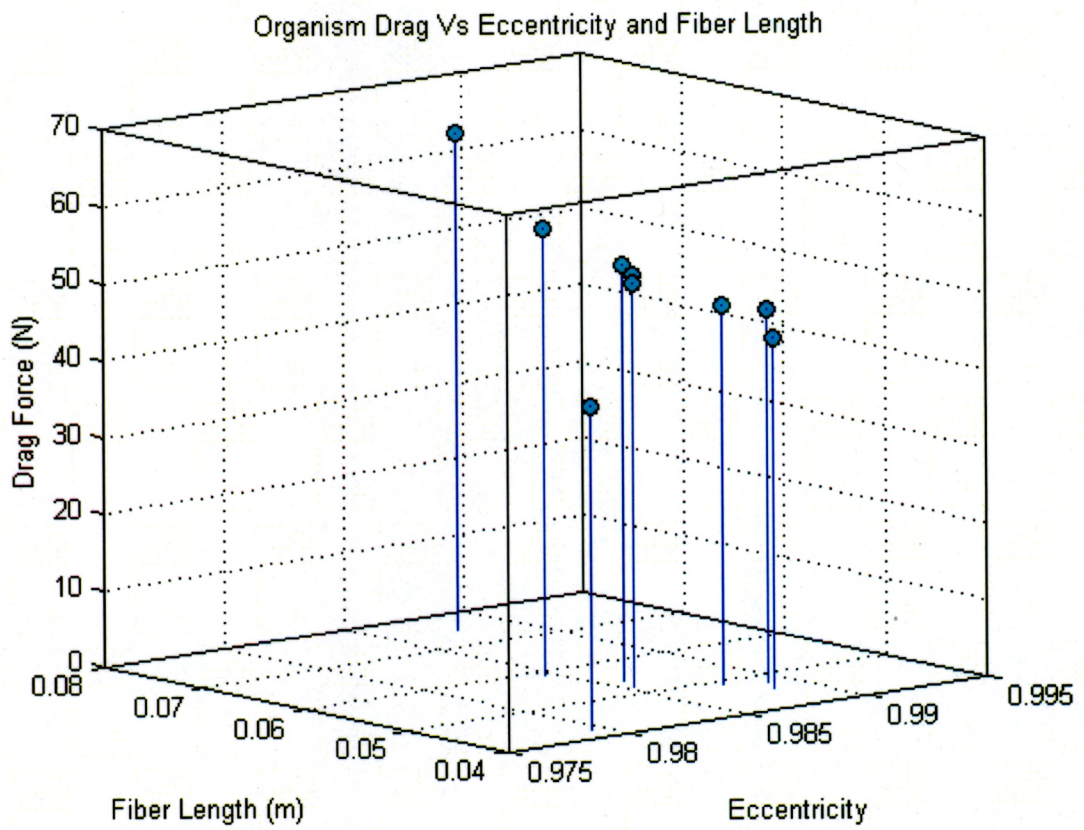


Figure 5.11: Biological Model: Drag Vs Eccentricity and Fiber Length

Chapter 6

Conclusion

In summary, this thesis examines the configurations of flexible fibers in a flow field through experiments and two dimensional numerical modeling. The results show qualitative similarity between experiment and two dimensional numerical simulation. Our investigations reveal that the length, orientation, and the placement of the fiber cause significant changes to the drag that the system experiences and the resulting deformation that the fibers undergo. These investigations further reveal that the eccentricity of the elliptical body, though less influential than fiber length, orientation, and placement, still causes changes to the drag that the system experiences and the resulting deformation that the fibers undergo.

The length of the fibers cause significant changes to the drag that the system experiences and the resulting deformation that the fibers undergo. Ellipsoid-fiber systems with longer fibers experience significantly more drag and fiber deformation. While Ellipsoid-fiber systems with shorter fibers experience less drag and less fiber deformation. This makes sense as the drag force a system experiences has a linear relationship to the length

of the system.

The orientation, and the placement of the fibers cause significant changes to the drag that the system experiences and the resulting deformation that the fibers undergo. Systems with fibers oriented with the flow experience less fiber deformation than than systems with fibers oriented either into the flow or perpendicular to the flow. Likewise, systems with fibers oriented with the flow experience less drag on the system when compared to systems with fibers oriented either into the flow or perpendicular to the flow. Meanwhile, systems with fibers which are placed in the wake of the ellipsoidal body experience an increase in the drag on the system and a greater degree of fiber deformation compared with systems whose fibers are at the same orientation and placed outside the wake of the ellipsoidal body.

The eccentricity of the elliptical body, though less influential than fiber length, orientation, and placement, still causes changes to the drag that the system experiences and the resulting deformation that the fibers undergo. All other factors being held equal, the systems with a more highly eccentric body will experience lower drag and less fiber deformation compared to their less eccentric counterparts. However, the length, orientation, and placement of the fibers are the driving forces behind the drag that the system experiences, and the deformation that the fibers undergo. Systems with highly eccentric bodies and long fibers will experience greater drag and more fiber deformation than systems with less eccentric bodies and short fibers.

Putting all these findings together, we can conclude that more streamlined systems will experience less drag than less streamlined systems. Likewise, fibers attached to more streamlined systems will experience less deformation than fibers attached to less

streamlined systems. This is a fairly intuitive finding, we naturally expect bodies that have to travel through a fluid to be streamlined. For example, fish have highly eccentric bodies and short fins. Likewise, birds have very narrow and elongated bodies.

Several significant questions remain and will be addressed in future reports on this subject. These include (i) the effects of fiber length versus fiber orientation on drag. (ii) The effect of fiber length, orientation, and body eccentricity on the time dependent fluttering of the fiber at higher Reynolds numbers. (iii) The effect of body eccentricity on the wake structure of the flow past the fiber in steady and unsteady conditions. (iv) The effect a third fiber attached to the rear of the ellipsoidal body, representing a tail, has on the system. Furthermore, a more detailed study of eccentricity versus fiber length needs to be conducted in order to obtain a more complete picture of the effects that eccentricity and fiber length have on drag. Finally, past theoretical studies of this problem, though rigorous, have been conducted in the absence of an elliptical body structure. Creating a theoretical model of the flexible fiber problem that accounts for the existence of an elliptical body structure must also be addressed in future studies.

Bibliography

- [1] Alben, S., Shelley, M. and Zhang, J., Drag reduction through self-similar bending of a flexible body, *Nature*, 420, 479-481, 2002.
- [2] S. Alben, M. Shelley, and J. Zhang, How flexibility induces streamlining in a two-dimensional flow, *Physics of Fluids* 16 (5): 1694-1713, 2004
- [3] Barois, Thomas, and Emmanuel De Langre. Flexible Body with Drag Independent of the Flow Velocity. *Journal of Fluid Mechanics*, 735, 2013.
- [4] Batchelor, G.K., *An introduction to fluid dynamics*, Cambridge University Press, 2000.
- [5] Camassa, R., Chung, B.J., Howard, P., McLaughlin, R.M., Vaidya, A., Vortex induced oscillations of cylinders at low and intermediate Reynolds numbers, *Advanced in Mathematical Fluid Mechanics*, Ed. A. Sequeira and R.Rannacher, Springer Verlag, 2010.
- [6] Childress, S., *Mechanics of Swimming and Flying (Cambridge Studies in Mathematical Biology)*, Cambridge University Press, July 31, 1981.
- [7] Cortes, S., D. Guemes, and R. Avila. "Low Reynolds Number Flow Around a Flying Saucer Micro Air Vehicle." *Technical Papers and Presentations. COMSOL*, 2013.
- [8] Drag. *Dictionary.com. The American Heritage Science Dictionary. Houghton Mifflin Company.* (accessed: May 02, 2015).
- [9] Fields, S.B., Klaus, M., Moore, M.G. and Nori, F., Chaotic dynamics of falling disks, *Nature*, 388, 252-254, 1997.

- [10] Galdi G.P., and Vaidya A., Translational Steady fall of Symmetric Bodies in Navier-Stokes Liquid, with Application to Particle Sedimentation, *Journal of Mathematical Fluid Mechanics*, 3, 183-211, 2001.
- [11] Galdi, G., P., On the Motion of a Rigid Body in a Viscous Fluid: A Mathematical Analysis with Applications, *Handbook of Mathematical Fluid Mechanics*, Elsevier Science, Amsterdam, 653-791, 2002.
- [12] Gosselin, F., de Langre, E. and Machado-Almeida, B.A., Drag reduction of flexible plates by reconfiguration, *Journal of Fluid Mechanics*, 650, 319, 2010.
- [13] Hamershock, David M., Thomas W. Seamans, and Glen E. Bernhardt. "Determination of Body Density for Twelve Bird Species." *Ibis* 137.3, 424-28, 1995.
- [14] Harder, D., Speck, O., Hurd, C. and Speck, T. Reconfiguration as a prerequisite for survival in highly unstable flow-dominated habitats. *J. Plant Growth Regul.* 23, 98–107, 2004.
- [15] Huang L, Quinn SJ, Ellis PD, Williams JE., Biomechanics of snoring, *Endeavour*, 19(3):96-100, 1995.
- [16] Kirchoff, G., *Über die Bewegung eines Rotationskörpers in einer flüssigkeit*, *J. Reine Ang. Math. Soc.*, 71, 237-281, 1869.
- [17] Leal, L.G., Particle Motion in a Viscous Fluid, *Annual Review of Fluid Mechanics*, 12, 435-476, 1980.
- [18] Luhar, M. and Nepf, H.M., Flow induced reconfiguration of bouyant and flexible aquatic vegetation, *Limnology and Oceanography*, 56 (6), 2003-2017, 2011.
- [19] Lugt, H., Autorotation, *Annual Review of Fluid Mechanics*, 15, 123-147, 1983.
- [20] Miller, L. A., A. Santhanakrishnan, S. Jones, C. Hamlet, K. Mertens, and L. Zhu. Reconfiguration and the Reduction of Vortex-induced Vibrations in Broad Leaves. *Journal of Experimental Biology*, 215.15, 2716-727, 2012.

- [21] Mittal, R., Seshadri, V. and Udaykumar, H.S., Flutter, Tumble and Vortex Induced Oscillations, *Theoretical and Computational Fluid Dynamics*, **17**, 165–170, 2004.
- [22] L.B. Pedersen and J.L. Rosenbaum. *Current Topics in Developmental Biology*.85:23-61, 2008.
- [23] Peskin, C. S. and McQueen, D. M. Fluid dynamics of the heart and its valves. In *Case Studies in Mathematical Modeling: Ecology, Physiology, and Cell Biology*, 2nd edn (ed. Othmer, H. G., Adler, F. R., Lewis, M. A. and Dallon, J. C.), pp. 309-338. New Jersey: Prentice-Hall. 1996.
- [24] Schouveiler, L., Eloy, C. & Le Gal, P., Flow-induced vibrations of high mass ratio flexible filaments freely hanging in a flow. *Phys. Fluids* **17** (4), 047104-8, 2005.
- [25] Shelley, M.J. and Zhang, J., Flapping and bending bodies interacting with fluid flows, *Annual Rev. Fluid Mech.*, **43**, 449-465, 2011.
- [26] Slaughter, W.S., *The linearized theory of elasticity*, Birkhauser, 2002.
- [27] Tanabe, Y. and Kaneko, K., Behavior of falling paper, *Physical Review Letters*, **73**, 10, 1372-1376, 1994.
- [28] Vogel, S., Drag and flexibility in sessile organisms, *American Zoologist*, **24**(1), 37–44, 1984.
- [29] Vogel, S., Drag and reconfiguration of broad leaves in high winds, *Journal of Experimental Botany*, **40**(217), 941-948, 1989.
- [30] Vogel, S., *Leaves in the Lowest and Highest Winds: Temperature, Force and Shape*. *New Phytologist*, **183**.1, 13-26, 2009.
- [31] Willmarth, W.W., Hawk, N.E., Galloway, A.J. and Roos, F.W., *Journal of Fluid Mechanics*, **27**, 177–207, 1967.
- [32] Zhu, L., Viscous flow past a flexible fibre tethered at its center pint: vortex shedding, *J. Fluid Mech.*, **587**, 217-234, 2007.

Appendix A

Numerical Parameters: Equilibrium Configuration

Notation	Description	Values
H_d	Domain Height	0.18 [m]
L_d	Domain Length	0.5 [m]
h_{bar}	flag height	0.0005 [m]
l_{bar}	length of flag	0.06 [m]
Cx_{circ}	x coordinate of cylinder	0.09 [m]
Cy_{circ}	y coordinate of cylinder	0.09 [m]
r_{circ}	radius of cylinder	0.0125 [m]
ρ_s	density of solid	1000 [kg/m ³]
ν_s	Poisson ratio	0.4
μ_s	Shear modulus	0.7×10^9 [kg/(ms ²)]
Es	$2\mu_s(1+\nu_s)$ (Young's modulus)	-
ρ_f	fluid density	1000 [kg/m ³]
ν_f	Fluid kinematic viscosity	0.001 [m ² /s]
μ_f	$\nu_f \rho_f$ (fluid dynamic viscosity)	
U_{mean}	mean inlet flow	0.009-0.451 [m/s]
β	$\frac{\rho_s}{\rho_f}$	-
Ae	$\frac{Es}{\rho_f * U_{mean}^2}$	-
Re	$\frac{U_{mean} * 2r_{circ}}{\nu_f}$ (Reynolds number)	0-30,000
α	initial angle of the fiber	135°(225°), 90°(270°), 45°(315°)

Table A.1: The table lists the numerical values of parameters assumed in the Equilibrium Configuration numerical investigations.

Appendix B

Numerical Parameters: Optimal Body Shape

Notation	Description	Values
X_{radius}	Semi-Major Radius	0.0125 - 0.0333 (m)
Y_{radius}	Semi-Minor Radius	0.0047 - 0.0125 (m)
U_{mean}	Mean inlet flow	0.009 - 0.451 (m/s)
H_d	Domain Height	0.18 (m)
L_d	Domain Length	0.5 (m)
h_{bar}	Fiber Height	0.0005 (m)
l_{bar}	Fiber Length	0.04 (m)
Cx_{circ}	x coordinate of ellipse	0.09 (m)
Cy_{circ}	y coordinate of ellipse	0.09 (m)
ρ_s	Density of solid	1000 (kg/m ³)
ν_s	Poisson ration	0.4
μ_s	Shear modulus	0.7×10^9 (kg/(m s ²))
E_s	$2\mu_s(1 + \nu_s)$ (Young's Modulus)	-
ρ_f	Fluid density	1000 (kg/m ³)
ν_f	Fluid kinematic viscosity	0.001 (m ² /s)
μ_f	$\nu_f \rho_f$	-
β	$\frac{\rho_s}{\rho_f}$	-
Ae	$\frac{E_s}{\rho_f \cdot U_{mean}^2}$	-
Re	$\frac{U_{mean} 2Y_{radius}}{\nu_f}$ (Reynolds number)	0 - 312.5
α	Initial angle of the fiber	90°(270°), 45°(320°)

Table B.1: The table lists the numerical values of parameters assumed in the Optimal Body Shape numerical investigations.

Appendix C

High Definition Images

High Definition versions of the images in figure 11.

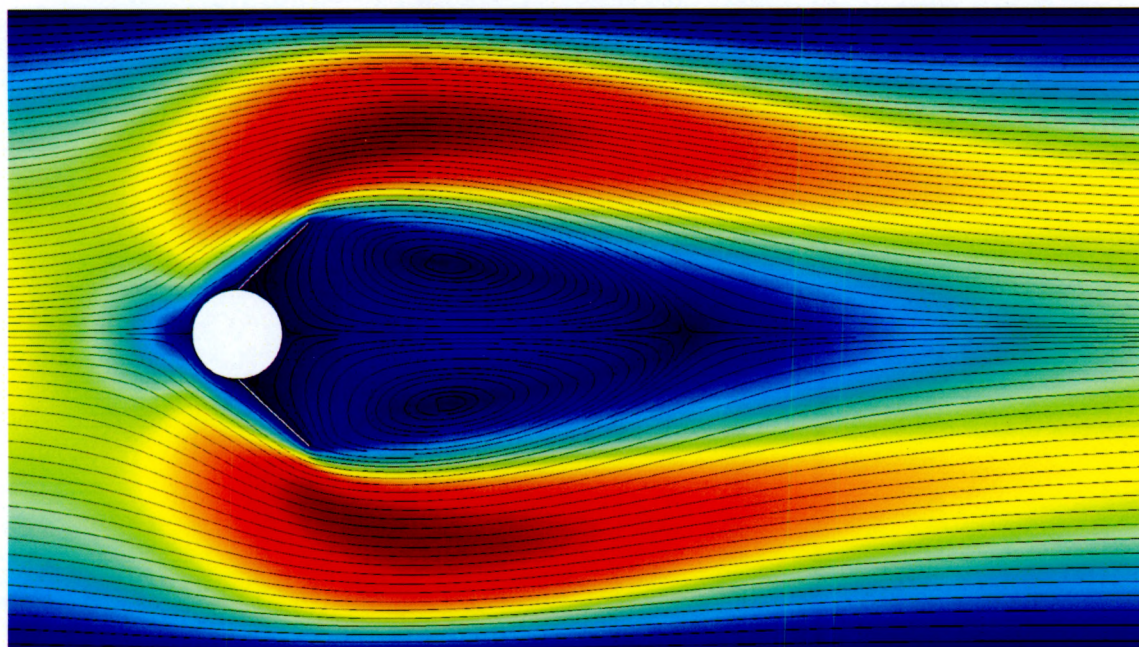


Figure C.1: 0.00 eccentricity model with fibers at 45° fixed along the edge, at time 5 seconds

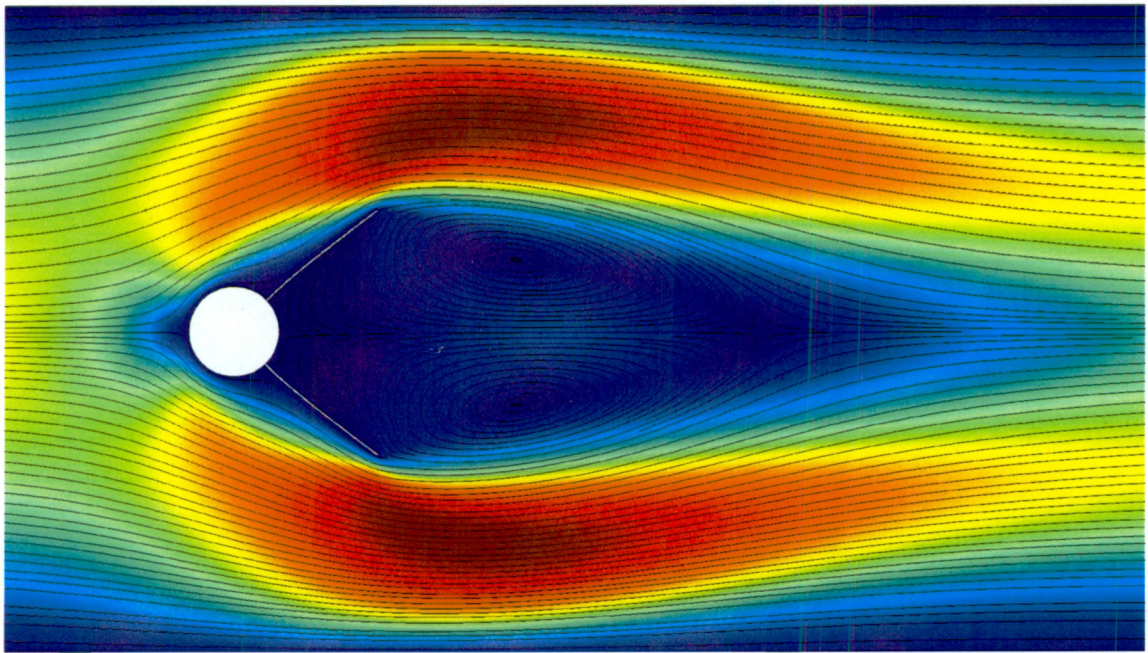


Figure C.2: 0.00 eccentricity model with fibers at 45° , at time 5 seconds

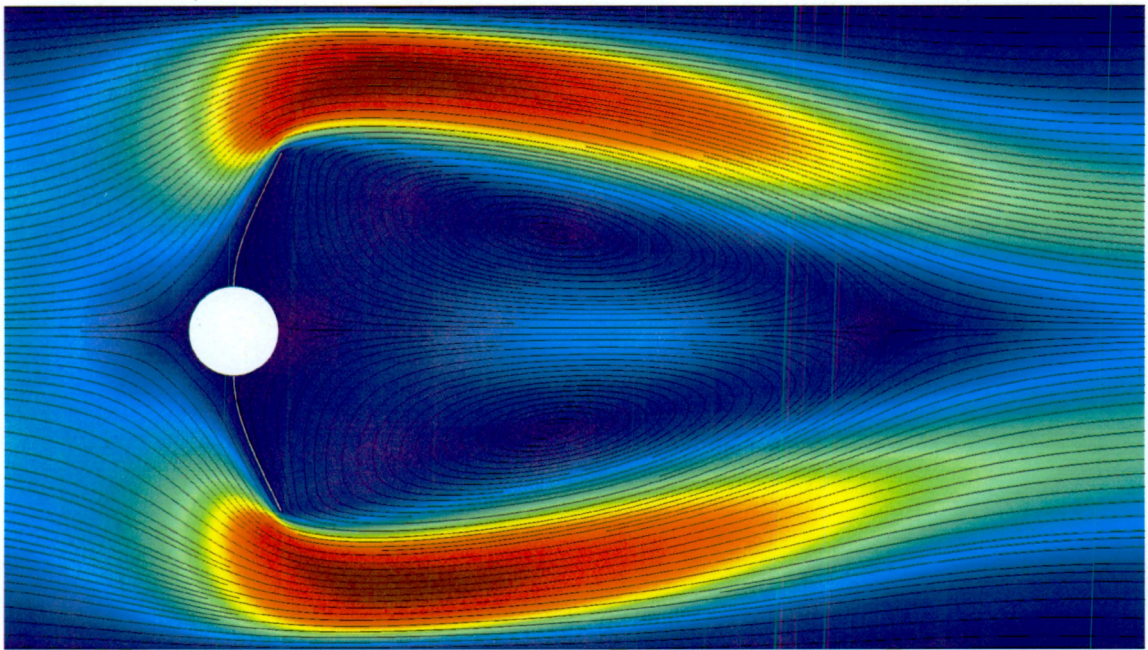


Figure C.3: 0.00 eccentricity model with fibers at 90° , at time 5 seconds

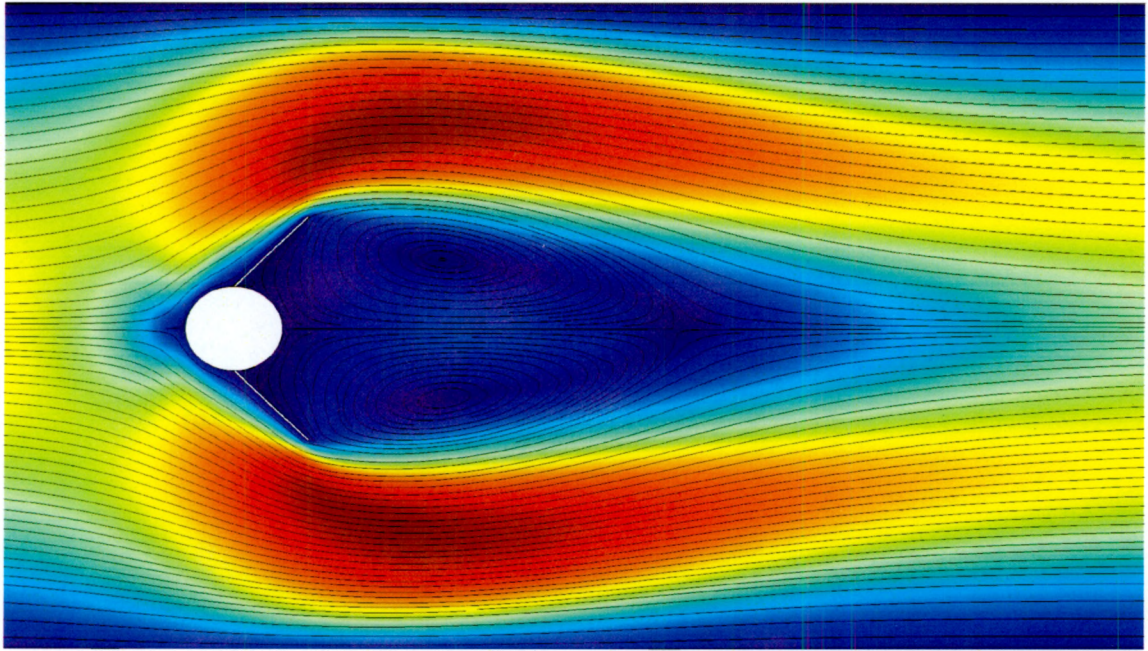


Figure C.4: 0.50 eccentricity model with fibers at 45° fixed along the edge, at time 5 seconds

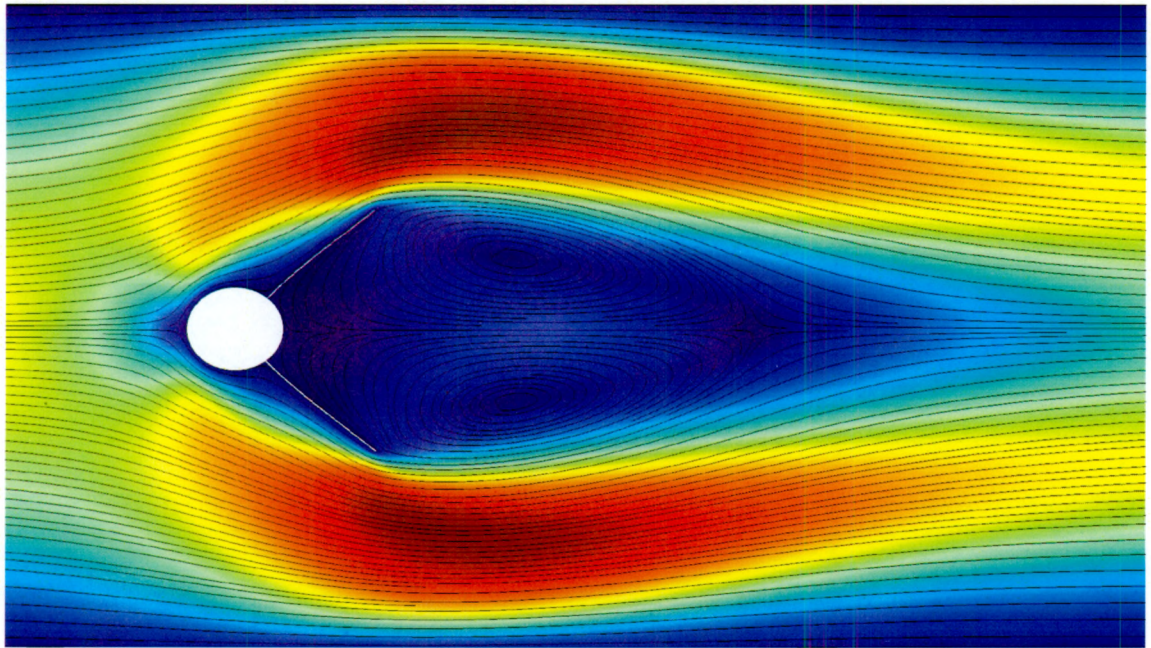


Figure C.5: 0.50 eccentricity model with fibers at 45° , at time 5 seconds

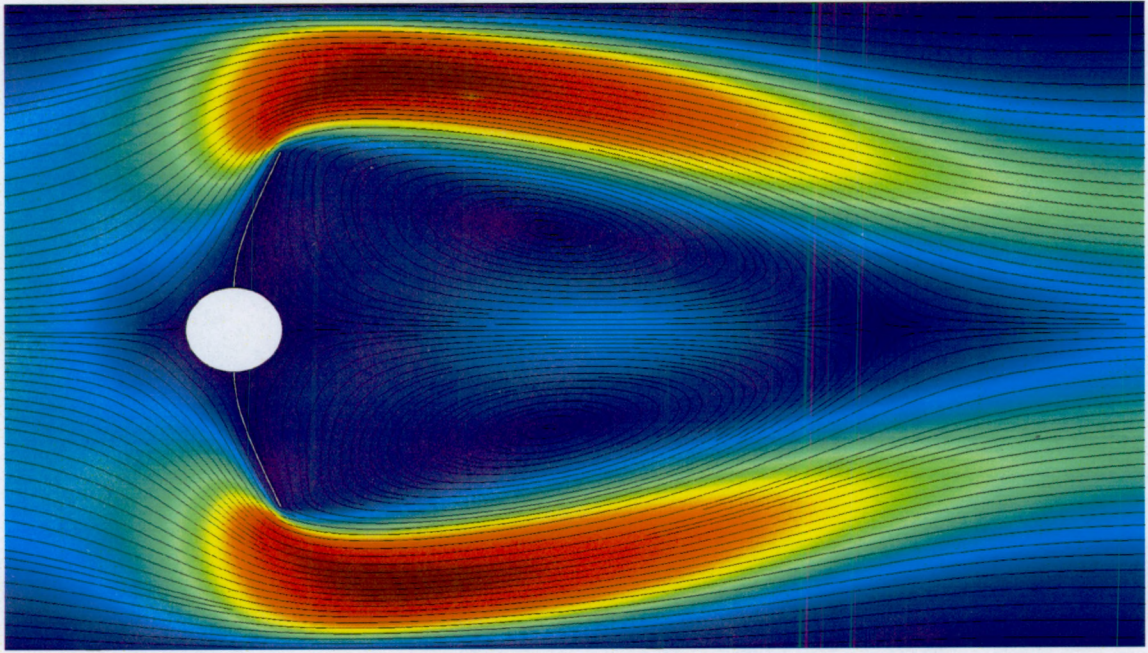


Figure C.6: 0.50 eccentricity model with fibers at 90° , at time 5 seconds

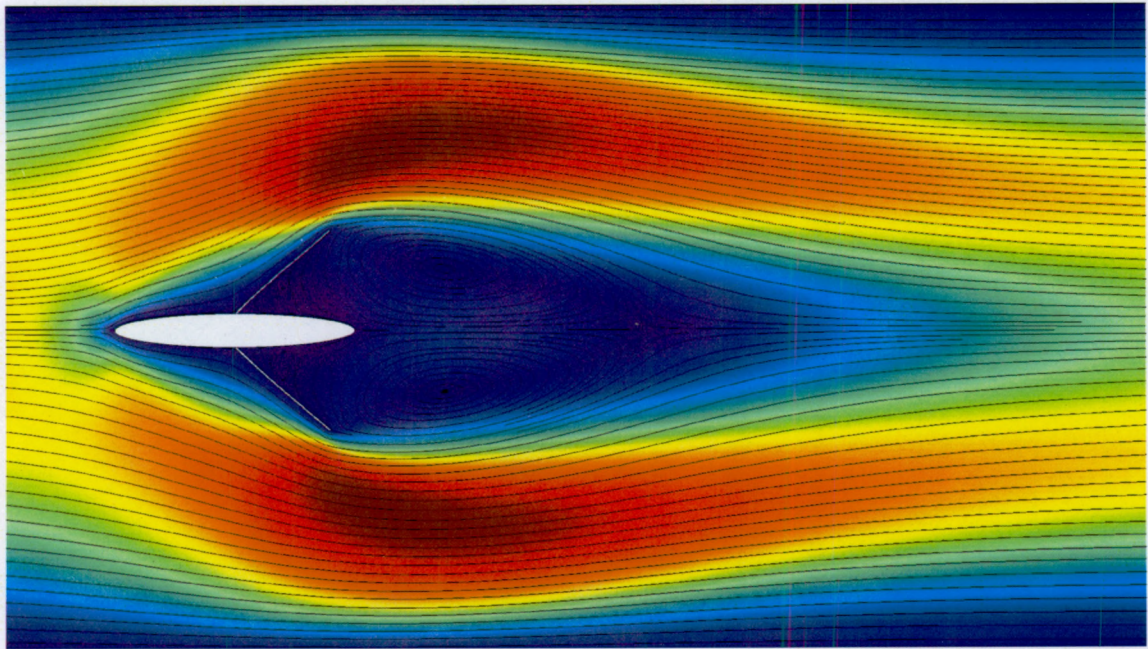


Figure C.7: 0.99 eccentricity model with fibers at 45° fixed along the edge, at time 5 seconds

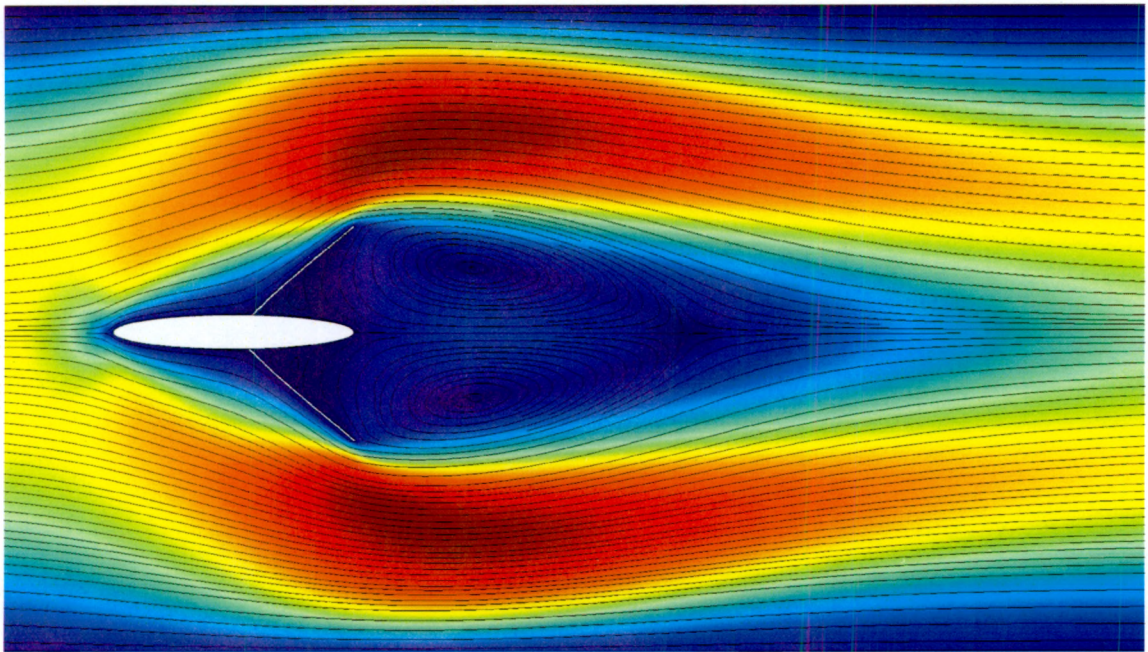


Figure C.8: 0.99 eccentricity model with fibers at 45° , at time 5 seconds

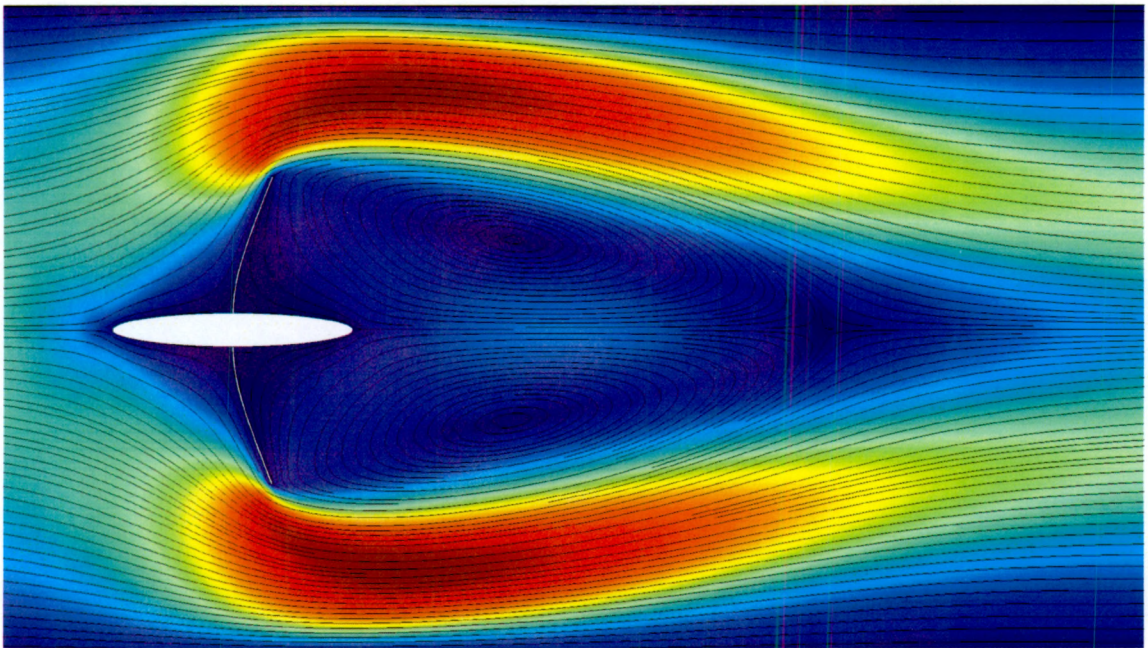


Figure C.9: 0.99 eccentricity model with fibers at 90° , at time 5 seconds

Appendix D

Bending Comparisons

Time	From Body	000ms	0.00ms	0.25ms	0.50ms	0.75ms	1.00ms	1.25ms	1.50ms	1.75ms	2.00ms	2.25ms	2.50ms	2.75ms	3.00ms	3.25ms	3.50ms	3.75ms	4.00ms	4.25ms	4.50ms	4.75ms	5.00ms	5.25ms	5.50ms	5.75ms	6.00ms	6.25ms	6.50ms	6.75ms	7.00ms	7.25ms	7.50ms	7.75ms	8.00ms	8.25ms	8.50ms	8.75ms	9.00ms	9.25ms	9.50ms	9.75ms	10.00ms										
000ms	0	0	0	0	0	0	0	0	0	0	0	0	0	0	0	0	0	0	0	0	0	0	0	0	0	0	0	0	0	0	0	0	0	0	0	0	0	0	0	0	0	0	0	0	0	0	0	0	0	0			
0.00ms	0	0	0	0	0	0	0	0	0	0	0	0	0	0	0	0	0	0	0	0	0	0	0	0	0	0	0	0	0	0	0	0	0	0	0	0	0	0	0	0	0	0	0	0	0	0	0	0	0	0	0	0	0
0.25ms	0	0	0	0	0	0	0	0	0	0	0	0	0	0	0	0	0	0	0	0	0	0	0	0	0	0	0	0	0	0	0	0	0	0	0	0	0	0	0	0	0	0	0	0	0	0	0	0	0	0	0	0	0

Appendix E

Drag Comparisons

